energies

MDPI

Article

A Novel Adaptive Control Approach Based on Available Headroom of the VSC-HVDC for Enhancement of the AC Voltage Stability †

Duc Nguyen Huu

Department of Renewable Energy, Faculty of Energy Technology, Electric Power University, 235—Hoang Quoc Viet, Hanoi 11355, Vietnam; ducnh@epu.edu.vn; Tel.: +84-901008555

† This paper is an extended version of our papers published in: Duc, N.H. Modeling and Analysis of an integrated AC-DC network under AC and DC faults. IEEE International Conf. on Sustainable Energy Technologies 2016. Duc, N.H. Small signal assessment of an AC system integrated with a VSC-HVDC network. IEEE EUROCON 2015.

Abstract: Increasing offshore wind farms are rapidly installed and planned. However, this will pose a bottle neck challenge for long-distance transmission as well as inherent variation of their generating power outputs to the existing AC grid. VSC-HVDC links could be an effective and flexible method for this issue. With the growing use of voltage source converter high-voltage direct current (VSC-HVDC) technology, the hybrid VSC-HVDC and AC system will be a next-generation transmission network. This paper analyzes the contribution of the multi VSC-HVDC system on the AC voltage stability of the hybrid system. A key contribution of this research is proposing a novel adaptive control approach of the VSC-HVDC as a so-called dynamic reactive power booster to enhance the voltage stability of the AC system. The core idea is that the novel control system is automatically providing a reactive current based on dynamic frequency of the AC system to maximal AC voltage support. Based on the analysis, an adaptive control method applied to the multi VSC-HVDC system is proposed to realize maximum capacity of VSC for reactive power according to the change of the system frequency during severe faults of the AC grid. A representative hybrid AC-DC network based on Germany is developed. Detailed modeling of the hybrid AC-DC network and its proposed control is derived in PSCAD software. PSCAD simulation results and analysis verify the effective performance of this novel adaptive control of VSC-HVDC for voltage support. Thanks to this control scheme, the hybrid AC-DC network can avoid circumstances that lead to voltage instability.

Keywords: adaptive control system; offshore wind energy; reactive power booster voltage; voltage stability; VSC-HVDC

Citation: Huu, D.N. A Novel Adaptive Control Approach based on Available Headroom of the VSC-HVDC for Enhancement of the AC Voltage Stability. *Energies* **2021**, *14*, 3222. https://doi.org/10.3390/en14113222

Academic Editor: Mario Marchesoni

Received: 22 April 2021
Accepted: 29 May 2021
Published: 31 May 2021

1. Introduction

VSC-HVDC technology is a promising solution for integration of future offshore wind farms into the existing AC system and also an attractive bulk power transmission structure in the next-generation networks [1]. VSC-HVDC can contribute to voltage stability improvement during severe disturbance [2–13], while the control schemes of the VSC-HVDC play an important role in the enhancement of the voltage stability [2–7,10–13]. In recent years, there are a number of research efforts focusing on the voltage stability of multi-terminal HVDC networks [2–13]. In [2], the AC grid is considered as a simplified mode, thus the dynamics interactions between the VSC-HVDC and the AC network are not counted. This study investigates the capacity transferring power of the AC line when applying different AC voltage control strategies. A reactive-power control strategy of VSC-HVDC for enhancement of power system transients is proposed in [4]. In this control scheme, a supplementary reactive power reference is added to the actual reactive power reference. An adaptive supplementary damping control based on the goal representation

heuristic dynamic programming (GrHDP) is introduced in [5]. In [6], the impact of loads on the voltage stability is studied by modeling loads as exponential load and induction motor, while the dynamics of the AC network were neglected. In the above-mentioned research, the improvement of voltage stability by using the VSC-HVDC networks is analyzed qualitatively with limited detailed analysis of VSC capacity.

It is also found that the control schemes of VSC have an important effect on the voltage stability. Several control methods of the VSC-HVDC networks to provide voltage enhancement during the AC voltage drops are presented in [5–13]. However, in those papers, the limits of the reference reactive current are always selected corresponding to different control modes, which will restrict the capability of VSC for reactive support, especially under serious voltage falls. Authors of [9] investigate the stability of an interconnected AC/DC network through adjustment of the VSC-MTDC operating point according to Hopf Bifurcation theory.

In [10], the influence of VSC-HVDC for reactive power control on the stability of the AC grid is introduced. In this paper, three different reactive power control modes are presented, which are constant reactive power control, constant AC voltage control, and AC voltage margin control. The impact of these reactive control modes on transient angle stability of the AC grid as well as dynamic power angle stability of the AC system is studied. In this study, the authors focus only on angle stability of the AC system. The voltage stability was not discussed much in this research. Moreover, upper and lower values of the current limiter in the control scheme are fixed.

In [11], analysis of voltage regulation of VSC-HVDC on power system stability is investigated. In this study, the reference reactive current is determined by a $V-i_q$ characteristic curve based on the grid code of Spain. Additionally, a control design method based on fractional order control theory is used for design of an AC voltage controller. The reference reactive current is not automatically changed according to faults suddenly occurring in the AC grid. Additionally, the model of the test case system is still reduced, with only two VSC-HVDC connected to an AC voltage source.

In [12], a control system is developed to provide reactive power support under short-circuit faults of the AC network. The reactive current limit can be changed depending on operation modes. This control scheme employs three different operation modes depending on conditions of the AC system, namely conditions of steady state, infeed grid fault, sending end grid fault, and conditions of sending end grid fault which is not cleared in time. However, the reactive current limit in this control scheme is not automatically changed according to real conditions of the system. Decisions of grid operators are still required. In an operation mode for maximum reactive power, the control scheme will default to using the total capacity of VSC for reactive generation without taking care of the realistic frequency of the system. This can lead to the frequency worsening because of a shortage of active power. Additionally, this control system also requires a communication system receiving an external control signal. The case study of [12] is based on the transmission network of Denmark with only one VSC-HVDC link, and it is restricted to the realistic grid.

Therefore, it is necessary to develop a proper control approach of the multi-VSC-HVDC networks embedded in the AC system in order to automatically adjust the output reactive power depending on the real-time severe conditions of the system.

In this paper, a more realistic multi-VSC-HVDC system feeding into the electric power system of south Germany is established. In order to consider dynamics of the AC network, instead of using the ideal voltage source, synchronous generators are used. For analyzing the impact of loads, static loads and induction motors are employed. Furthermore, an adaptive control method of the VSC-HVDC networks is proposed to enhance the voltage support by automatically adjusting the reactive current limits while ensuring not to worsen the frequency of the system according to the dynamics conditions of the system. This results in the maximum utilization of the VSC capability for reactive power support. The key merit of this proposed adaptive control is automatically following to dynamic operation conditions of the AC network based on the system frequency. It therefore contributes to

improvement of voltage stability as well as angle stability of the AC system. As a result, effective operation of the AC grid embedded to VSC-HVDC links can be enhanced. In addition, this novel control method applied to a VSC operates without requirement of exchanging information with other VSC. This novel adaptive control could be described as "act locally but support globally". Finally, the simulation results realize the performance of the proposed adaptive control method.

The rest of the paper is organized as follows. Section 2 describes the VSC-HVDC system embedded in the representative AC system based on the south German network and its model. Section 3 presents the proposed adaptive control method of the VSC-HVDC system integrated with the AC network. Simulation results and discussion are analyzed in Section 4. Finally, the conclusions are drawn in Section 5.

2. Model of the Hybrid VSC-HVDC-AC System

The configuration overview of the sample hybrid VSC-HVDC-AC network, as shown in Figure 1, is used for analysis in this paper. This hybrid network is based on a reduced AC transmission network of Germany and is already presented in [14–16]. The system is composed of an overlay of multi-VSC-HVDC links and a representative AC network based on the transmission network in Germany. The overlay VSC-HVDC grid represents the planned HVDC lines to transfer power from projected offshore wind farms in the north to heavy load centers in the south of Germany. More detail of the representative AC network is provided in Appendices A–C. The represented hybrid AC-DC system is divided into regional AC grids, the overlay HVDC transmission grid, and three aggregated offshore wind farms in the north. Local loads and generating plants close together are grouped and considered as the regional load and generation sub-networks, respectively. The HVDC lines are underground cables. This system was built in PSCAD. It is composed of an overlay multi-VSC-HVDC including 7 VSC stations and 7 HVDC links, with the voltage level of 800 kV, 13 aggregated generators representing 13 regional AC generation grids, 3 aggregated wind farms, 16 transformers connecting with 13 generators and 3 wind farms, and 22 AC transmission lines with the voltage level of 380 kV. In order to consider dynamic behaviors of the AC network, synchronous generators, and AC transmission line with PI-models, the static loads and dynamic loads are adopted to model the AC network. Tables A3 and A4 in the Appendix list the main parameters of the AC network. Detailed modeling of subgroup units is described as follows.

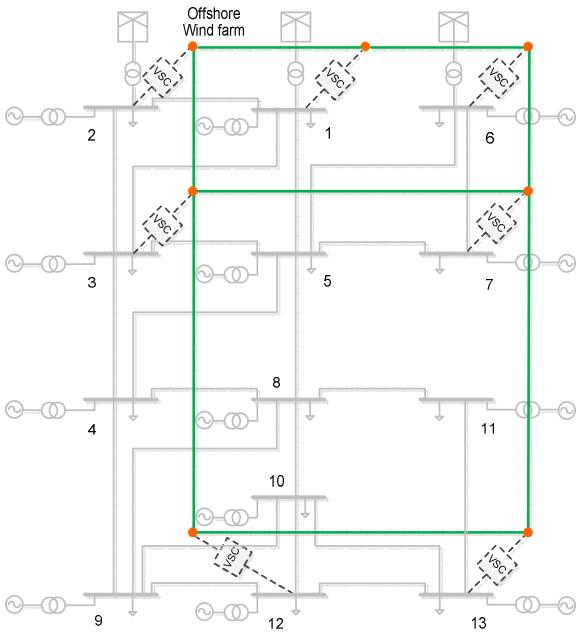

Figure 1. Configuration of the study hybrid VSC-HVDC-AC networks [15].

2.1. Model of The VSC-HVDC System

This section describes an overview of the main components of the VSC system and the average model.

2.1.1. Main Components of the VSC-HVDC System

The typical configuration of a VSC-HVDC is depicted in Figure 2. Main components of the VSC-HVDC include AC filters, transformers, coupling reactors, DC cables, DC capacitors, two three-phase VSCs, and their control systems. Transformers are normally used to transform the AC voltage to a proper level for the converters. Coupling reactors are used to control currents through them in order to control active and reactive flows. AC filters are employed to prevent harmonics caused by the switching of converters. DC cables are taken from [17]. DC capacitors are required to keep the power balance during transients and reduce the voltage ripple on the DC side and their size should be properly designed [18,19]. The two-level VSC and its average model are employed in this study.

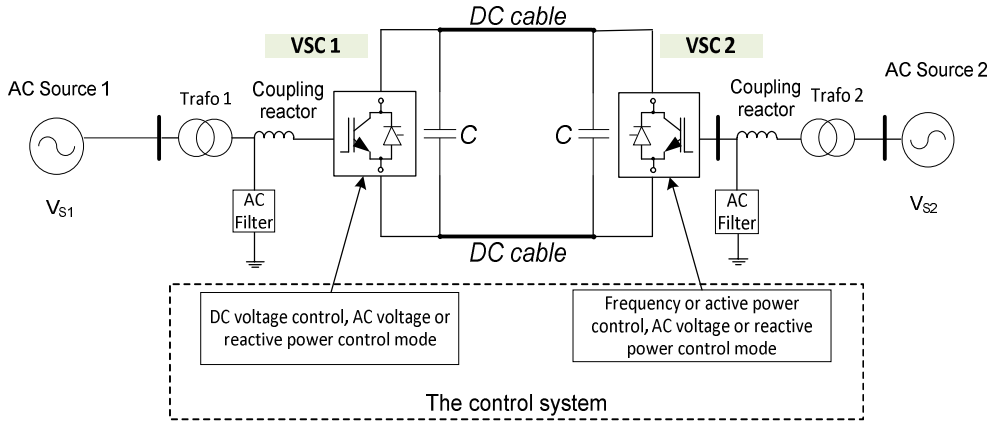

Figure 2. Typical configuration of a VSC-based HVDC.

Figure 2 shows a schematic diagram of a controlled-frequency VSC system whose kernel is a current-controlled VSC [20]. The VSC system can be considered as the composition of an ideal VSC, an equivalent DC-bus capacitor, and a DC voltage source which represents the DC transmission system. In the VSC system, each phase of the VSC AC-side terminals is interfaced with a regional AC subsystem via an interface AC filter. The AC filter includes a resistor in series with inductor and a shunt capacitor with capacitance C_f. The filter provides a low-impedance path for switching current harmonics generated by the VSC and thus prevents them from penetrating into the AC subsystem. The current-controlled VSC and the filter capacitor deliver the real and reactive power (P_s, Q_s) and (0, Q_c), respectively. Therefore, the effective power output of the VSC system exchanged to the AC network is (P_s, Q_s + Q_c). $V_{t,abc}$ and V_{sabc} are the AC voltages at the terminal and PCC respectively, $i_{L,abc}$ are the current flowing to the AC network, r_{on} denotes the switch on-state resistance of VSC, while R and L are resistance and inductance at AC side of VSC, and ρ is the output of PLL.

2.1.2. The Average Model of the VSC System

There are several representations of the hybrid AC-DC for the purpose of modeling and control system. Of those choices, representation of the AC system in the *dq0* coordination system facilitates the control. In comparison with *abc*-frame control, the *dq0* control reduces the number of plants to be controlled from three to two. Furthermore, instantaneous decoupled control of active and reactive power, which is exchanged between the VSC system and the AC system, can be implemented. Additionally, one of the merits of the *dq0* control is that the control variables are DC quantities in steady state so that zero

steady-state error is readily achieved [21]. This advantage is important for compensator design, especially in cases that frequency can change.

$$V_j(t) = \frac{1}{2} V_{dc}(t) m_j(t),\ j = a, b, c \tag{1}$$

where m_j is achieved from the *dq0-abc* transformation of the reference voltage, V_{ctrol}. Neglecting losses in the VSC system, as seen in Figure 3, the power balance between the DC and AC side is written as:

$$P_{dc}(t) = V_{dc}(t) I_{dc}(t) = \sum v_j(t) i_j(t) = P_{ac}(t) \tag{2}$$

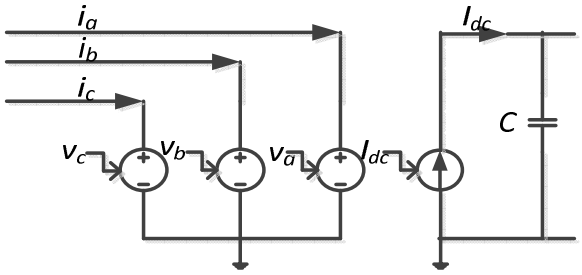

Figure 3. Average model diagram of the VSC system [16].

From (1) and (2), the controlled current on the DC side can be determined as:

$$I_{dc}(t) = \frac{1}{2} \sum i_j(t) m_j(t) \tag{3}$$

Otherwise, the controlled current on the DC side can be derived in the *dq0* frame. The real and reactive power exchanged to the AC subsystem at the PCC (the point of common coupling) are determined as:

$$P_s(t) = 1,5\left[V_{sd}(t) i_d(t) + V_{sq}(t) i_q(t)\right] \tag{4}$$

$$Q_s(t) = 1,5\left[-V_{sd}(t) i_q(t) + V_{sq}(t) i_d(t)\right] \tag{5}$$

where V_{sd} and V_{sq} are the AC system *dq0* frame voltages. As a consequence, the controlled current on the DC side can be computed as:

$$I_{dc}(t) = \frac{3}{2V_{dc}} \left[V_{sd}(t) i_d(t) + V_{sq}(t) i_q(t)\right] \tag{6}$$

DC filters and measurement filters are not taken into account in the average model.

2.2. Model of the AC System

The AC side includes regional AC subsystems and offshore wind farms. The regional generation subsystems are represented by the aggregated synchronous generators [22]. Aggregated offshore wind farms are modeled as in [22]. For the problem of voltage stability analysis, the static loads and dynamic loads are modeled in order to consider dynamic responses. Main parameters of the test case AC grid are provided in the Tables A2–A4 in the Appendix.

2.2.1. Model of Synchronous Generator

The synchronous generator consists of an excitation system and a turbine system. The model of the excitation system adopts the IEEE V2 Compatible Solid-State Exciter (SCRX19) [23–26]. The output field voltage is regulated by a control scheme to keep the

voltage of the system unchanged at V_{ref}. The nomenclature in the block diagram of the exciter system, shown in Figure 4, is as follows:

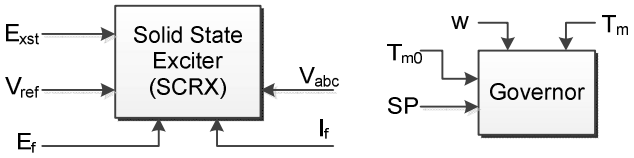

Figure 4. Block diagram of the exciter and governor model.

V_{ref}: The reference voltage in per-unit, which the exciter acts to control.

I_f: The field current received from the machine in per-unit. It applies to the negative current logic.

V_{abc}: Receives input from the node loop component.

E_{xst}: Input to modify V_{ref} and is suitable for connecting a power system stabilizer.

E_f: This output is the computed field voltage applied directly to the synchronous machine. The V2 compatible hydro-governor model [23,24] is used in this study. Inputs of the model include the reference speed (SP), mechanical torque from the machine (T_{m0}), and machine rotor speed (w). The output is the mechanical torque (T_m). It is also noted that the ability of regulating the terminal voltage is limited by the capacity of generating the reactive power margin. In the studied system, the power factor of the generator is kept at 0.85.

2.2.2. Model of Components in AC Side

To consider dynamic behavior of loads, static loads and induction motors are used.

The static loads are represented by the exponential load model, which can be expressed as follows:

$$P = P_0(\frac{V}{V_0})^{NP}(1 + K_{PF}.dF) \quad (7)$$

$$Q = Q_0(\frac{V}{V_0})^{NQ}(1 + K_{QF}.dF) \quad (8)$$

where P and Q are the equivalent active and reactive power of the load when the bus voltage magnitude is V, P_0 and Q_0 are rated active and reactive power of the load at the voltage magnitude of V_0, and NP, NQ, K_{PF}, and K_{QF} denote the characteristics of the load with voltage and frequency respectively, which can be typically chosen as $NP = NQ = 2.0$, $K_{PF} = 1$, $K_{QF} = -1$.

AC transmission lines are modeled as a Pi-model. Parameters R, L, and C of AC lines are lumped and listed in Table A3. A model of a 3-phase, 2-winding transformer is used in this study based on the classical modeling approach [27].

2.3. Model of HVDC Transmission Lines

Underground DC cables should be used for DC transmission lines because of reasons coming from technical and public opinion aspects [28]. The model of DC transmission lines derived in the study is represented as a π model. Each DC cable is denoted by a number of π models in series depending on its distance, as shown in Figure 5. The acceptable number of these pi sections will be investigated and determined.

Figure 6 depicts the comparison of the impedance spectra of the Pi-model with the distributed model of 800 kV, 500 km-long cable. It is obviously noted that more pi sections will give better results but have more computational burden. It is shown that with four pi-sections, a close approximation of DC transmission lines is considered adequate.

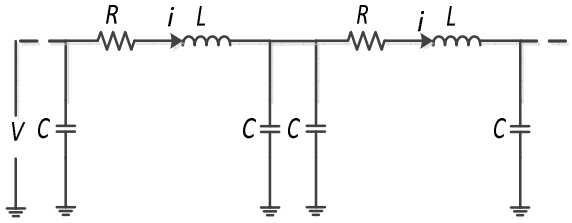

Figure 5. Model of cascaded pi-section DC transmission lines.

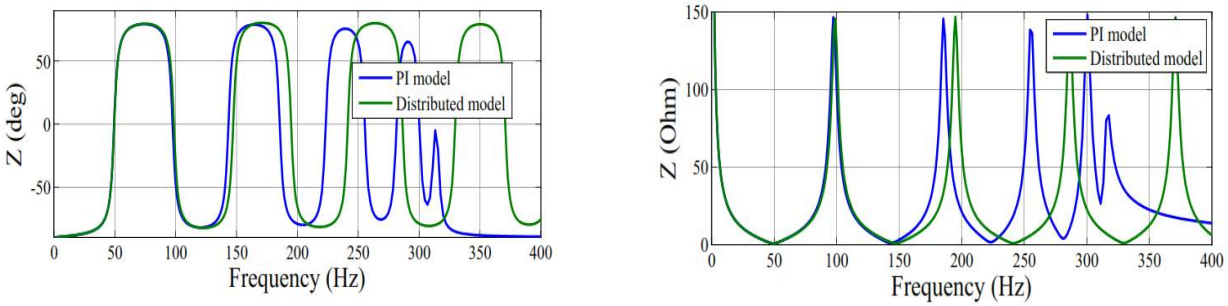

(**a**) (**b**)

Figure 6. Comparison of the impedance spectra of a 800 kV, 500 km−long cable with a distributed model and cascaded pi-section model: (**a**) Impedance phase angle, (**b**) impedance magnitude [15].

2.4. Model of Wind Farms

Figure 7 describes the configuration of an aggregated wind farm [22]. PMSG is used in this study. Wind farm includes a block of wind speed model, wind turbine, wind generator, three-phase transformer, as well as the control system. Detailed modeling of wind farms is derived from previous publications [14–16,22]. Modeling of wind farms is briefly introduced in Appendix B.

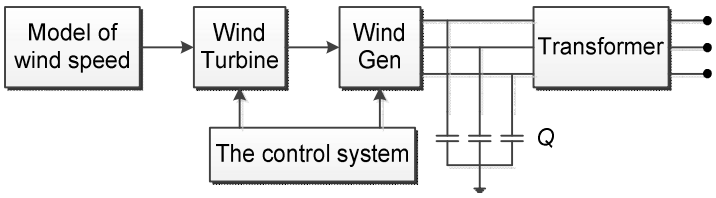

Figure 7. The model of the wind farm unit.

3. A Novel Adaptive Control for the Multi-VSC-HVDC System

In this section, the control method of a multi VSC-HVDC is presented and analyzed. The control scheme applied to one VSC-HVDC as well as the coordinate control strategy for a multi-terminal VSC-HVDC system is introduced.

The control system of the VSC system shown in Figure 8 can be classified into an outer control loop, an inner control loop, and a phase-locked loop (PLL). The outer controller is designed to provide the reference currents for the inner controller. The inner controller regulates the currents, keeping track of reference currents, and also decouples the d- and q-axes in order to control active and reactive currents independently. The function of PLL is to regulate the $\omega(t)$ for synchronization with the AC system voltage. Since the scope of this research focuses on the control system of the VSC-HVDC, the aforementioned main control loops will be discussed in the following subsections.

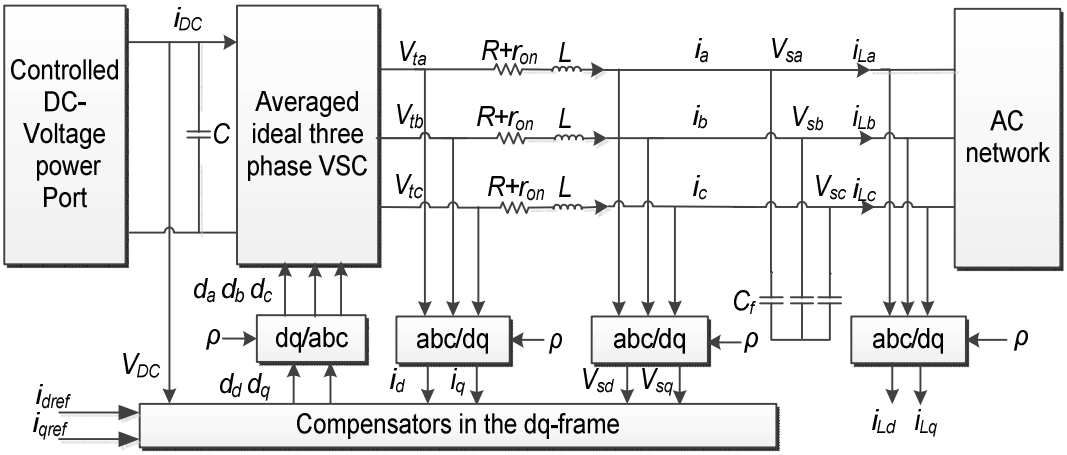

Figure 8. The control scheme of the VSC.

3.1. The Inner Control Loop

One of the purposes of the control system is to regulate the instantaneous real and reactive power at the PCC ($P_s(t)$ and $Q_s(t)$). Normally, there are two methods to achieve this goal [21]. The first method, deployed mainly in flexible alternating current transmission systems' (FACTS) controllers, is the voltage-mode control approach [29,30]. In this way, the real and reactive power are regulated by the relationship between the magnitude and the phase of the VSC AC side terminal voltage and that of the PCC voltage [31]. The merit of this method is that it is simple and has a low number of control loops [30]. However, since the VSC line current is not directly controlled, the VSC cannot be protected against over-currents, especially when there is a fault in the AC network. To overcome this demerit, the second method, which is called "current-mode control", forces the VSC AC side current to be controlled, as shown in Figure 9. In this control scheme, the amplitude and phase of the VSC line current with respect to the PCC voltage are used to control both active and reactive power. Furthermore, the current-mode control method provides robustness against variations in parameters of the VSC as well as the AC system, better dynamic performance, and higher control precision than the first approach [32]. Figure 9 depicts the control system diagram of the VSC based on the second method in *dq0* frame. A decoupling control is employed to control active current and reactive current independently. A conventional PI controller is used, where an integral part is necessary to avoid a steady-state error. The resulting control equations are written as follows. The list of the symbols can be found in the list of nomenclature at the end of the manuscript.

$$u_{\mathrm{dq}} = K_{\mathrm{P,dq}}(i_{\mathrm{dqref}} - i_{\mathrm{dq}}) + \int K_{\mathrm{I,dq}}(i_{\mathrm{dqref}} - i_{\mathrm{dq}})dt \tag{9}$$

$$V_{\mathrm{td}} = u_{\mathrm{d}} + V_{\mathrm{sd}} - \omega_0 L i_{\mathrm{qref}} \tag{10}$$

$$V_{\mathrm{tq}} = u_{\mathrm{q}} + V_{\mathrm{sq}} - \omega_0 L i_{\mathrm{dref}} \tag{11}$$

$$d_{\mathrm{d}} = (u_{\mathrm{d}} + V_{\mathrm{sd}} - \omega_0 L i_{\mathrm{qref}})/V_{\mathrm{DC}} \tag{12}$$

$$d_{\mathrm{d}} = (u_{\mathrm{d}} + V_{\mathrm{sd}} - \omega_0 L i_{\mathrm{qref}})/V_{\mathrm{DC}} \tag{13}$$

$$V_{\mathrm{ctrl\_d}} = V_{\mathrm{td}} - V_{\mathrm{sd}} + \omega_0 L i_{\mathrm{q}} \tag{14}$$

$$V_{\mathrm{ctrl\_q}} = V_{\mathrm{tq}} - V_{\mathrm{sq}} - \omega_0 L i_{\mathrm{d}} \tag{15}$$

$$\frac{di_{\mathrm{dq}}}{dt} = -\frac{R_s}{L_s} i_{\mathrm{dq}} + \frac{1}{L_s} V_{\mathrm{ctrl\_dq}} \tag{16}$$

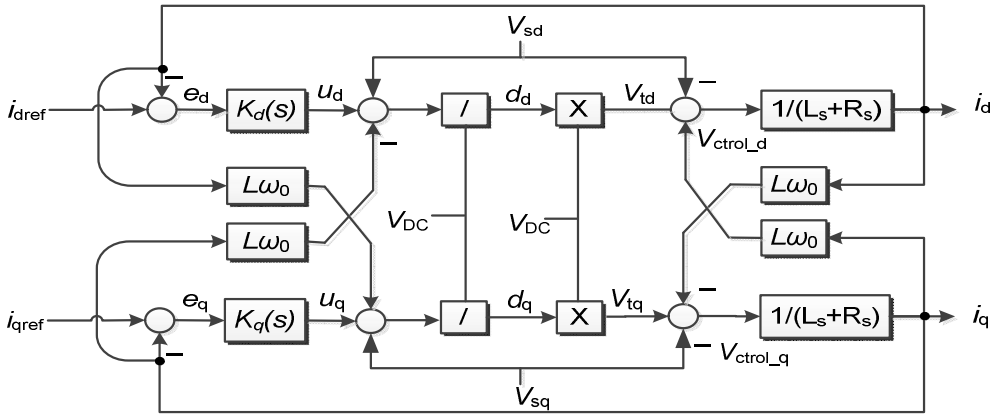

Figure 9. Control block diagram of the current-controlled VSC [16].

3.2. The Outer Control Loop

The aim of the outer control loop is to generate the current references for the inner current control loop. Depending on the different control objectives, the active current reference can be achieved through either active power control loop or DC voltage control loop. In the VSC-HVDC link, one VSC is to control active power, while the other one is to control DC voltage. The reactive current reference can be obtained from either reactive power or AC voltage control loop depending on the strength of the AC system that connects to the VSC-HVDC link.

In the steady state, thanks to the PLL $V_{sq} = 0$, therefore, Equations (4) and (5) can be rewritten as:

$$P_s(t) = 1,5V_{sd}(t)i_d(t) \tag{17}$$

$$Q_s(t) = -1,5V_{sd}(t)i_q(t) \tag{18}$$

Based on Equations (17) and (18), it is obvious that active and reactive power can be controlled by i_d and i_q, respectively. Therefore, the reference currents for the inner controller can be determined as:

$$i_{dref}(t) = \frac{2}{3V_{sd}} P_{sref}(t) \tag{19}$$

$$i_{qref}(t) = \frac{2}{3V_{sd}} Q_{sref}(t) \tag{20}$$

where i_d, i_q, and V_d, V_q are the currents and voltages at the AC grid side in the d-axis and q-axis, respectively.

- The DC droop control scheme

It is also noted that in the current-mode control approach, the DC voltage should be constant, thus the VSC system exists as a bidirectional power flow path between the AC side and the DC side. Yet, in this study, the DC bus voltage varies during disturbance, and therefore, it needs to be controlled. Consequently, it is important to develop the control system taking into account both the active and DC bus voltage control, as shown in Figure 10. From the literature, DC bus voltage control can be broadly divided into two categories, namely, the master-slave and DC droop control [33]. The main disadvantage of the former is that operation of the DC network as well as the hybrid AC/DC system relies on the normal operating condition of the VSC controlling DC voltage. This leads to immediate outage of the system when the VSC responsible for controlling DC bus voltage is disconnected. The latter should use more than one VSC system to control the DC bus voltages, which has been presented in several publications [34–38]. Hence, when a disconnection of one VSC in the droop control scheme occurs, the remaining part of the system will continue to function normally. Thus, the reliability of the system is improved.

For these reasons, the DC droop control scheme is used for the multi-VSC-HVDC systems in this study.

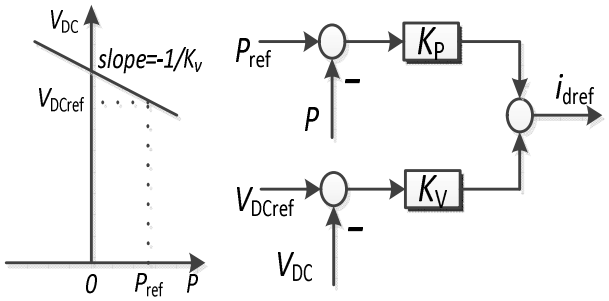

Figure 10. The DC voltage droop control configuration and the corresponding DC voltage versus power characteristic [16].

- Control the AC voltage $V_{s,abc}$ at the PCC

When a disturbance occurs in the AC system, for instance a three-phase short circuit, which results in large changes of the voltage at the PCC of the AC system, the objective of the control system is to control the amplitude subsystem voltage, $V_{s,abc}$. Additionally, V_{sd} and V_{sq} in *dq0* frame can be controlled in order to regulate the amplitude of the AC voltage. The control scheme applied for the VSC is presented in Figure 11, in which V_{sd} and V_{sq} can be regulated by i_{dref} and i_{qref}, respectively.

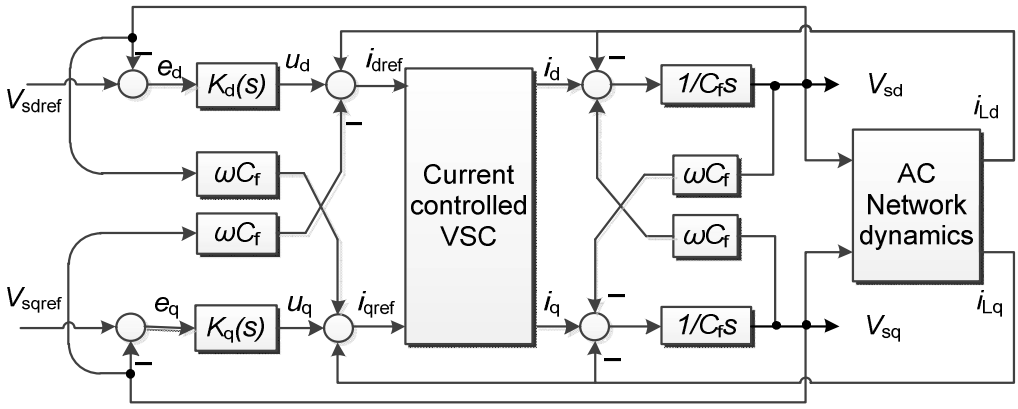

Figure 11. Control block diagram of the VSC controlling $V_{sabc.}$

The inner control loop is the current-mode controller that is already presented in the previous section, shown in Figure 9. The additional equations describing the outer control loop are as follows:

$$u_{dq} = K_{P2,dq}(V_{sdqref} - V_{sdq}) + \int K_{I2,dq}(V_{sdqref} - V_{sdq})dt \quad (21)$$

$$i_{dref} = u_d + i_{Ld} - \omega C_f V_{sq} \quad (22)$$

$$i_{qref} = u_q + i_{Lq} + \omega C_f V_{sd} \quad (23)$$

$$\frac{dV_{sd}}{dt} = \frac{1}{C_f}(i_d + \omega C_f V_{sq} - i_{Ld}) \quad (24)$$

$$\frac{dV_{sq}}{dt} = \frac{1}{C_f}(i_q + \omega C_f V_{sd} - i_{Lq}) \quad (25)$$

3.3. The PLL

The function of PLL is to regulate $\omega(t)$ for synchronization with the AC system voltage [39]. The PLL employs a negative feedback control system that regulates ρ at (ω_0t + θ_0) and is composed of three main components: the error signal calculator, the compensator, and the voltage-controlled oscillator (VCO). The control system diagram of the PLL is depicted in Figure 12. The equation describing the PLL can be expressed as follows:

$$\frac{d\rho}{dt} = V_s H(p)(\omega_0 t + \theta_0 - \rho) \tag{26}$$

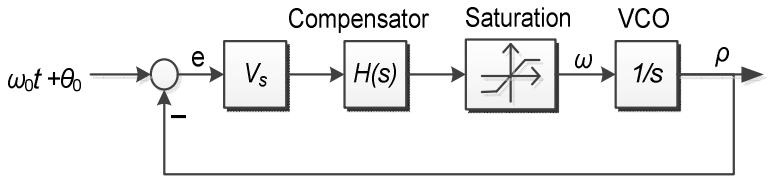

Figure 12. The control diagram of the PLL.

In (26), $H(p)$ is a transfer function and the limitations of $\omega(t)$ should be chosen properly to allow excursions of $\omega(t)$ during transients.

3.4. Concept of Adaptive Current Controller

It is obligatory to have a current limiter for VSC in order to protect over-current fault. A current limiter will keep reference active and reactive currents determined by the outer control loop in permitted ranges and provide for the inner control loop, as shown in Figure 13. The maximum reference current limit of the VSC can be expressed as:

$$i_{\text{lim}} = K_{\text{lim}} i_{\text{rated}} \tag{27}$$

where K_{lim} is the parameter that reflects the ability of the VSC for the over-current trip (usually selected as 1.5 [40]), and i_{rated} is the nominal current of VSC. The limit current is composed of two components in *dq0* frame: an active current limit and a reactive current limit, which can be defined as:

$$i_{\text{lim}} = \sqrt{i_{\text{dlim}}^2 + i_{\text{qlim}}^2} \tag{28}$$

where i_{dlim} and i_{qlim} are limit values of active and reactive currents, and their values are determined by different control schemes. In [12], limit values of reactive currents are changed based on operation modes of the system as well as specific applications.

For the conventional control strategies, fixed or preset values of the limit current of VSC are typically calculated according to control modes, and it does not consider the actual capacity and hence the available capacity amount of VSCs for stabilizing the AC voltage during transients caused by different kinds of contingency. In our study, the current controller margins of the VSC, namely i_{dlim} and i_{qlim}, will be automatically changed according to dynamic frequency of the AC system, which will be expressed in the following paragraph, as shown in Figure 13. It is seen in Figure 14 that there are several current limit values depending on different operation schemes of the VSC-HVDC, as follows:

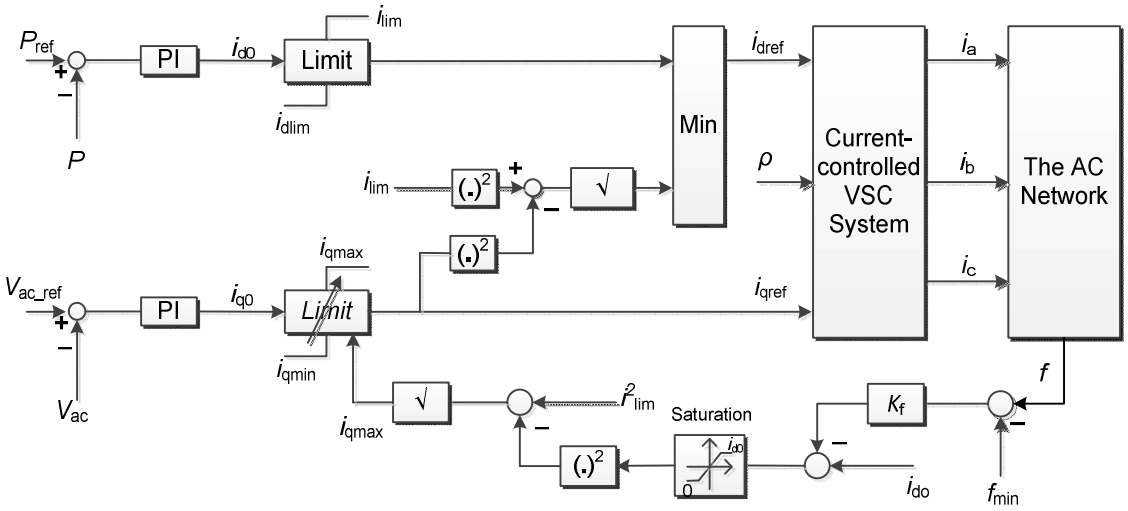

Figure 13. Block diagram of the dynamic reactive power booster applied to the VSC-HVDC system.

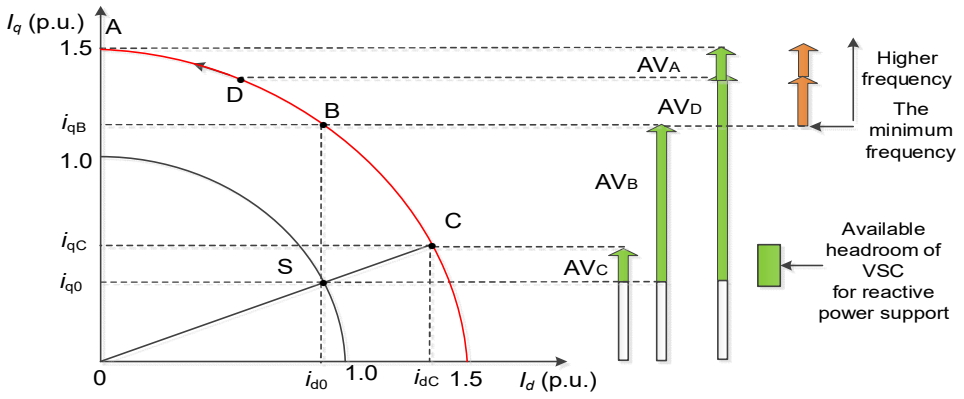

Figure 14. Concept of adaptive current limits based on available headroom of VSC.

In a conventional control scheme, the current limit of VSC is chosen at the point C corresponding to the steady-state point S. In this control scheme, the available headroom of VSC for reactive power support is denoted by AR_C, as seen in Figure 14.

In our proposed adaptive control system, the current limit is dynamically adjusted within the range from point C to point A, depending on the real-time frequency of the AC system. If the real-time frequency is equal to the required minimum frequency (determined by the grid code), the current limit is at point B according to the available headroom of VSC, denoted by AR_B. In realistic operation scenarios of the grid, the AC frequency can be higher, which can lead to the available headroom of VSC for reactive power support, AR_D. As a result, the proposed adaptive controller can maximally utilize the available headroom of VSC for the highest reactive power support.

It is noted that in order to transfer desired active power in steady-state operation, the lower limit of the active current must be at least equal to the nominated active current. Therefore, in the conventional control method, the upper limit of the reactive current in such traditional control strategies can be calculated as:

$$i_{\text{qlim\_max}} = \sqrt{i_{\text{lim}}^2 - i_{\text{rated}}^2} = \sqrt{(1.5 i_{\text{rated}})^2 - i_{\text{rated}}^2} = 1.12 i_{\text{rated}} \quad (29)$$

With the different operation strategies, the current reference limits are set at different set-points, as depicted in Figure 13, which provides the different current controller margins of the VSC. Consequently, it can be concluded that with existing control methods, the reactive current limit of the VSC is pre-fixed, which restricts the enhancement of the voltage

support during sudden faults of the system. Therefore, it is essential to develop a control approach so that the voltage stability is automatically improved within the capacity of VSC.

3.5. Dynamic Reactive Power Booster

From the above analysis, in order to exhaust the capacity of VSC to enhance the voltage support under voltage drops, instead of fixing limit values of the reference current, an adaptive control method applied to the VSC-HVDC is proposed, as shown in Figure 13, and it allows to automatically regulate the limits according to the dynamics change of the frequency during severe faults. This proposed control scheme is composed of an outer control loop, an inner current controller, and an adaptive current controller for automatically achieving maximum reactive power support while ensuring to not make the change of the frequency worse during voltage drops and the outer control loop. This control approach can be called a dynamic reactive power booster.

The core concept is based on available headroom of VSC in order to automatically change the limits of the reactive current reference in order to increase voltage support while ensuring minimal effect on the frequency under unexpected operation conditions of the system. The dynamic reactive power booster can be described as follows.

First, the limits of the reference reactive current are calculated according to dynamic changes of the frequency (the realistic condition of the system), as:

$$i_{\mathrm{df}} = i_{\mathrm{d0}} - K_{\mathrm{f}}(f - f_{\mathrm{min}}) \tag{30}$$

$$i_{\mathrm{q\_max}} = \sqrt{i_{\mathrm{lim}}^2 - i_{\mathrm{df}}^2} \tag{31}$$

$$i_{\mathrm{q\_min}} = -i_{\mathrm{q\_max}} \tag{32}$$

Second, the reference reactive current can be determined as:

$$i_{\mathrm{qref}} = \begin{cases} i_{\mathrm{q0}}\,, & i_{\mathrm{q\_min}} < i_{\mathrm{q0}} < i_{\mathrm{q\_max}} \\ i_{\mathrm{q\_max}}\,, & i_{\mathrm{q0}} \geq i_{\mathrm{q\_max}} \\ i_{\mathrm{q\_min}}\,, & i_{\mathrm{q0}} \leq i_{\mathrm{q\_min}} \end{cases} \tag{33}$$

Finally, the reference active current can be derived as:

$$i_{\mathrm{dref}} = \begin{cases} i_{\mathrm{d0}}\,, & i_{\mathrm{dlim}} < i_{\mathrm{d0}} < i_{\mathrm{d\_comp}} \\ i_{\mathrm{d\_comp}}\,, & i_{\mathrm{d\_comp}} \leq i_{\mathrm{d0}} \\ i_{\mathrm{dlim}}\,, & i_{\mathrm{d0}} \leq i_{\mathrm{dlim}} \end{cases} \tag{34}$$

where $i_{\mathrm{d\_comp}}$ can be determined as:

$$i_{\mathrm{d\_comp}} = \sqrt{i_{\mathrm{lim}}^2 - i_{\mathrm{qref}}^2} \tag{35}$$

where i_{d0}, i_{qo} are provided by the outer control loop, i_{dref}, i_{qref} are the actual reference current signal determined by the dynamic reactive power booster, i_{lim} is the maximum permitted current of VSC, i_{dlim} is the lower permitted value of the active current, $i_{\mathrm{q\_max}}$ is the dynamic limit of the reactive limiter, and $i_{\mathrm{d\_comp}}$ is the signal which will be compared with i_{d0}. K_{f} is the parameter depending on the system and it should be properly chosen.

The selection of the parameter K_{f} can be basically determined as follows:

$$K_{\mathrm{f}} = \frac{\Delta P_{\mathrm{sys,max}}}{\Delta f_{\mathrm{sys,max}}} \times \frac{2}{3V_{\mathrm{sd}}} \tag{36}$$

$$\Delta P_{\mathrm{sys,max}} = P_{\mathrm{sys,max}} - P_{\mathrm{sys}}^0 \tag{37}$$

$$\Delta f_{\mathrm{sys,max}} = f_{\mathrm{sys}}^0 - f_{\mathrm{min}} \tag{38}$$

where $P_{sys,max}$ is the maximum active power that the system can generate in primary control, P^0_{sys} and f^0_{sys} are generated active power and nominal frequency of the system in steady state, f_{min} is the permitted minimum frequency of the system, and V_{sd} is the d-axis AC voltage of the system connected to VSC.

The flow chart algorithm of this proposed dynamic reactive power booster based on available headroom of VSC is shown in Figure 15.

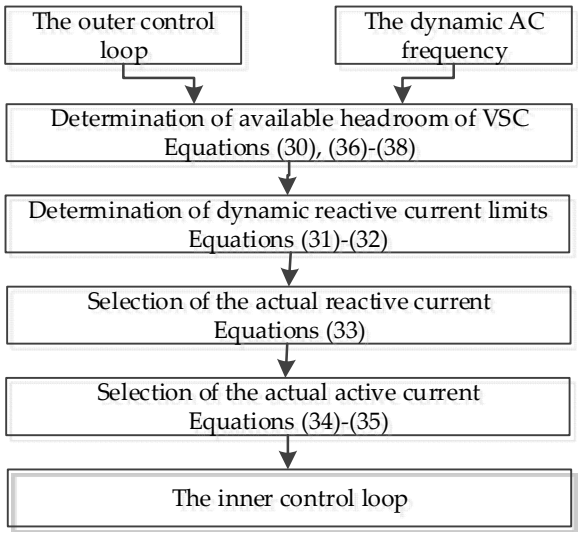

Figure 15. The flow chart algorithm of the proposed dynamic reactive power booster.

It is worth noting that with pre-fixed values of current limits, the reference reactive current must be lower than $1.12i_{rated}$, as discussed in Section 3.4. In contrast, with the proposed dynamic reactive power booster, the reference reactive current can reach up to i_{lim} (here it is chosen as $1.5i_{rated}$). The dynamic reactive power booster automatically generates the limits according to the realistic dynamics condition of the system.

3.6. Feasibility Analysis of the Proposed Dynamic Reactive Power Applied to the Multi-VSC-HVDC System

It is important to mention that with the proposed dynamic reactive power booster, the reference active current is dynamically regulated according to the change of the frequency in order to realize maximum voltage support. Therefore, it is necessary to evaluate the AC network response when applying this proposed method. It is possible to further reduce the suppled active power to increase the available headroom of VSC for reactive power support if the frequency of the system is still within the permitted lower limit. Thus, the frequency is not worse when applying the proposed control method.

Furthermore, since the required active power of load deceases during AC voltage drops, the supplied active power of VSC can be reduced. Hence, available headroom of VSC for reactive power can significantly increase. Moreover, the inertia energy in the AC network can help to maintain the frequency within a reasonable limit. Consequently, this dynamic reactive power booster will not lead to larger deviation of the frequency nor cause instability of frequency.

Since this adaptive control scheme does not require a communication system, it can individually work locally and automatically but still globally support the problem of voltage stability. In addition, this approach does not change the specific control strategies applied to VSC-HVDC in normal conditions, it only modifies the existing control schemes by adding a so-called dynamic reactive power booster, as shown in Figure 15.

4. Simulation Results and Discussion

In this section, several time domain simulations with different test cases will be implemented in order to realize the effective performance of the proposed method. In addition, investigation of small signal stability will be analyzed to study the effects of the adaptive control approach on small signal stability of the system. The more realistic study network shown in Figure 1 is built and simulated in PSCAD/EMTDC. The parameters of the system are listed in the Appendix, in Tables A1–A8.

4.1. Investigation of Small Signal Stability

In order to investigate the effects of the adaptive control method on the stability of the system, it is necessary to first linearize the nonlinear models such as WECS, AC sub-grids, and VSC-HVDC including the adaptive control before analysis. The small signal model of the hybrid AC-DC system is taken from [16] and forms a state model with the 110th order. The parameters of the system are listed in Appendix C. In normal operation, one of its objectives is to transfer a total of 18 GW from offshore wind power parks in the north to load centers in the south. The total load of the system is 24 GW, and the rest of the demand is supplied by synchronous generators. It is assumed that small disturbances occur when a pulse change is applied to P_{ref} of the converter 1. Different control strategies applied for VSC, including the master-slave, the DC voltage droop control, and AC voltage control, are studied.

The state equations of the system in Figure 1 can be properly written in matrix form as in (39), and the output of the system is defined as in Equation (40):

$$\dot{x} = f(x, u, t) \tag{39}$$

$$y = g(x, u, t) \tag{40}$$

Linearizing the state equations of the system, including the proposed method around the steady-state operating point, the small-signal model of the system can be defined as follows:

$$\dot{\widetilde{x}} = A\widetilde{x} + B\widetilde{u} \tag{41}$$

$$\widetilde{y} = C\widetilde{x} + D\widetilde{u} \tag{42}$$

where $\widetilde{x} = x - x_s$, $\widetilde{u} = u - u_s$ and $\widetilde{y} = y - y_s$, and where the subscript "s" denotes the steady-state values and matrix A, B, C, D are defined as:

$A = \frac{\partial f}{\partial x}|x_s, u_s$; $B = \frac{\partial f}{\partial u}|x_s, u_s$; $C = \frac{\partial g}{\partial x}|x_s, u_s$; $D = \frac{\partial g}{\partial u}|x_s, u_s$. Based on matrix A, B, C, D, the eigenvalues of the system can be calculated. The characteristic equation of A is defined as:

$$\det(A - \lambda I) = 0 \tag{43}$$

where I is an identity matrix of appropriate dimensions and λ is the system eigenvalues of the matrix A.

- Analysis of the impact of the control parameters on the system stability

As VSC systems are extremely fast-response power electronic devices, therefore, their control parameters must be appropriately chosen in a great effort to improve the stability of the system. The eigenvalue analysis is performed to study the impact of the control parameters on the stability. The majority of the eigenvalues are associated with VSC subsystems, as shown in Figure 16a. Some dominant eigenvalues in per-unit with respect to 50 Hz are listed in Table 1. Figure 16c describes the change of direction of the eigenvalues with the change of the gain of the DC voltage controller K_{pa}. The gain of the DC voltage controller in the outer loop K_{pa} is increased from 3 to 30. It can be seen in Figure 16c that the higher K_{pa} will result in higher frequency oscillations in transients as well as a decrease the margin of the stability. It is also noted that when K_{pa} is larger than 52, there are some eigenvalues moving into the right side of the plane, making the system unstable.

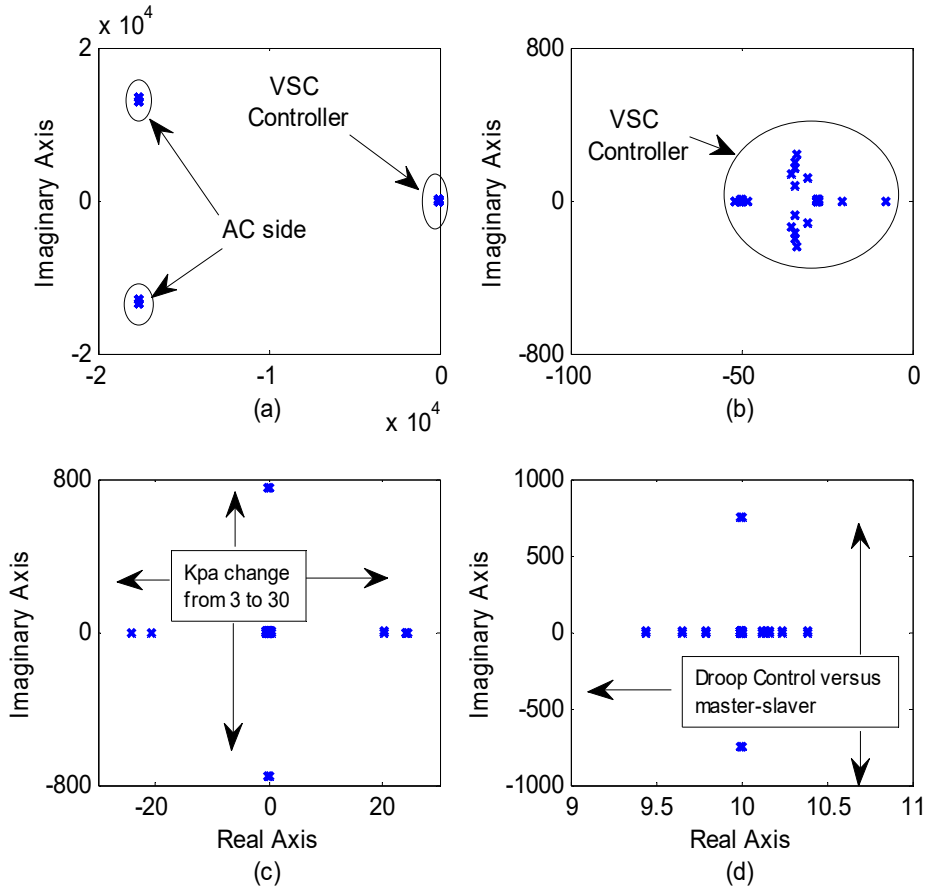

Figure 16. (**a**) Eigenvalues of the system, (**b**) some dominant eigenvalues of VSC, (**c**) difference between eigenvalues of the system in case of K_{pa} = 30 and in case of K_{pa} = 3, and (**d**) difference between eigenvalues of the system in case of the droop control and in case of the master-slave [16].

Table 1. Some dominant eigenvalues when K_{pa} = 3 [16].

Eigenvalues	Damping Ratio	Frequency (Hz)
$-0.323 \pm 4.890i$	0.0659	38.913
$-0.318 \pm 3.915i$	0.0810	31.154
$-0.292 \pm 2.728i$	0.1064	21.709
$-0.388 \pm 2.424i$	0.1581	19.289
$-0.310 \pm 1.525i$	0.1992	12.136

- Analysis of the DC voltage control strategies

In order to see the influence of the DC voltage control method on the stability, an eigenvalue analysis of the performance of the two control schemes was carried out. The first control scheme is the master-slave DC voltage control (only one VSC connected to node 1 control DC voltage), and the other method is the DC voltage droop control. It is shown in Figure 16d that the magnitude of eigenvalues in the imaginary axis increases in the second scheme, while the magnitude of eigenvalues in the real axis decreases only slightly. This means that the stability margin of the system in the second control method is better than that of the first method. Additionally, with the DC voltage droop control, the reliability of the system is improved. In conclusion, the second strategy performs fast, with very low overshot, and it is superior to the first strategy.

- Analysis of the stability of the system when the VSC-HVDC participates in control AC voltages

The disturbance is seen as a 10% decrease of the AC voltage at the PCC 4. On the condition of other system parameters remaining unchanged, the gain of the AC voltage controller K_{pa} is increased from K_0 to 50 K_0 ($K_{pa} = 2.6 \times 10^{-4}$). It is shown in Figure 17 that when the gain of the AC voltage controller increases, some eigenvalues will move close to the imaginary axis. Therefore, the stability margin of the system will be reduced. When K_{pa} = 60 K_0 (equal to 0.0157), some eigenvalues are at the right side of the imaginary axis, thus the system would be unstable, as shown in Figure 17b.

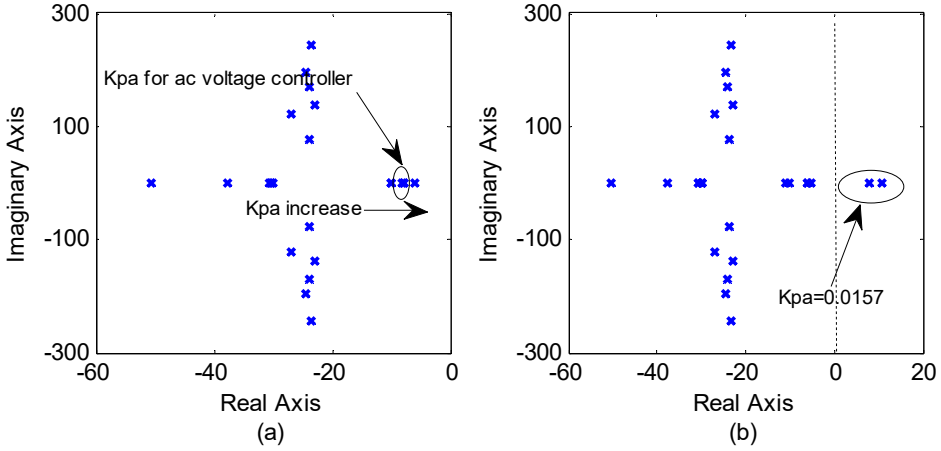

Figure 17. Analysis of eigenvalues-locus in case of AC voltage control method: (**a**) $K_{pa} = 2.6 \times 10^{-4}$, (**b**) $K_{pa} = 0.0157$.

4.2. Verification of the Proposed Dynamic Reactive Power Booster in Voltage Support

Case study: Three-phase-to-ground fault at the transmission line between bus 12 and bus 13.

A three-phase-to-ground fault at the transmission line between bus 12 and bus 13 is applied at a time of 20 s and is cleared by CB_1 and CB_2 0.1 s later. A reclosure is carried out at 20.7 s. This case study is performed in order to investigate one of the most stressed faults causing the deep drop of AC voltage.

The initial operating conditions of the system are assumed as follows:

- The aggregated synchronous generators generate 0.85 p.u. active power to the transmission grid.
- The terminal voltage magnitudes of generators are set as 1.05 p.u.
- The aggregated wind farms supply 0.8 p.u. active power rating to the system.
- The VSC-HVDC transfers 0.8 p.u. active power to the AC network.
- The maximum current of VSC is set at 1.5 times the nominated current.
- The conventional method is operated according to the point "C" control scheme, as shown in Figure 13.
- The AC transmission lines 10–13 and 11–13 reach near limits on transferring power.
- The induction motor represented for dynamic loads is connected to bus 13.

It is noted that voltage stability problems are closely related to load characteristics that rely on the characteristics of load and operating induction motors and are heavily sensitive to varied voltages. Thus, induction motors are typically used for voltage stability analysis.

Simulation results show the comparison between the proposed dynamic power booster approach and the conventional control method operating at point C, as seen in Figure 13. Figure 18 shows the transients of the system in case of a three-phase-to-ground fault occurring at the AC transmission link from bus 12 to bus 13. It is seen in Figure 18a that the voltage at bus 13 drops to nearly zero after the fault happens. The rotor speed of the induction motor decreases because of the mismatch between the electromagnetic torque and the mechanical torque, as shown in Figure 18c. It is noted that the capacity of the VSC connected to node 13 will reduce significantly when the AC voltage at bus 13 drops. Figure 18e shows the dynamics of the active power supplied by the VSC connecting

bus 13 with different control strategies. Figure 18f demonstrates the effective reactive power support of the VSC thanks to the dynamic reactive power booster. It is realized that with the proposed dynamic reactive power booster, the reference reactive current limit is varied automatically, according the dynamics of the system frequency. It can be seen that the system frequency is in the range of its limits, as shown in Figure 18d. Consequently, utilization of the VSC's capacity is implemented to maximum AC voltage support, while at the same time ensuring the AC frequency within a permitted range. Hence, this control scheme can achieve both key objectives, as (1) improvement of the voltage stability based on available headroom of its VSC and (2) keeping the angle stability in reasonable consideration.

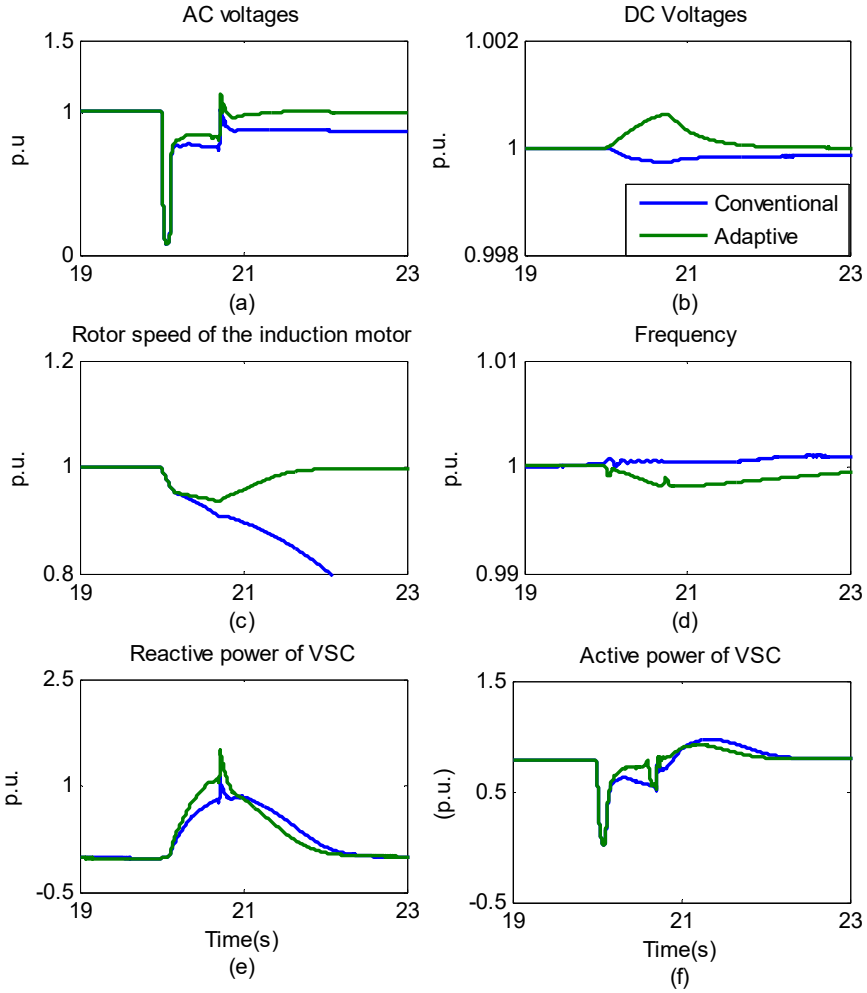

Figure 18. Verification of the proposed control method in case of AC voltage support: (**a**) dynamics of AC voltages at bus 13; (**b**) dynamics of DC voltages connected to node 13; (**c**) rotor speed of the induction motor; (**d**) dynamics of the system frequency; (**e**) dynamics reactive power of VSC connected to node 13; (**f**) dynamics active power of VSC connected to node 13.

When the fault is cleared at a time of 20.1 s, the voltage begins to bounce back. It is obviously seen that in comparison with the conventional control method, the voltage recovery is better than with the proposed adaptive control method. Hence, the maximum reactive power support of the VSC can be achieved while ensuring not to make the system frequency worse. As a result, the dynamic reactive power booster scheme provides the best voltage recovery and prevents speed decrease of the induction motor, as shown in Figure 18a,c.

4.3. Realization of the Proposed Control Method Following Faults

In order to realize the proposed control method following faults on the AC and DC sides and outages of VSCs, the following cases are simulated and analyzed:

- *Case 1:* An outage of the generator 2
- *Case 2:* An outage of the AC line 12 in the AC network
- *Case 3:* An outage of the DC line 37
- *Case 4:* An outage of the VSC 1

In simulation, the droop control scheme is applied for VSC-HVDC networks. VSC_1, VSC_2, and VSC_3 systems are planned to transfer total offshore wind, 18 GW, in the north to VSC_4, VSC_5, VSC_6, and VSC_7. The reactive power control is set to zero. The control system of three aggregated offshore wind farms is used to extract wind energy under the MPPT scheme.

A. AC-side faults

Figure 19 depicts the dynamics behavior of the system when a trip of generator 2 happens at time of 25 s. The dynamics of the system when a trip of AC line 12 occurs at a time of 25 s is shown in Figure 20. It is seen that penetration of these trips into the DC grid is very small. From these simulation results, it is also shown that the VSC-HVDC acts as a network firewall against cascading disturbances happening in AC sides. This is achieved thanks to automatic reduction of current and power in the event of faults. It is also noted that in these cases, the dynamic reactive power booster is not activated because the actual reactive current still does not reach the dynamic limit value.

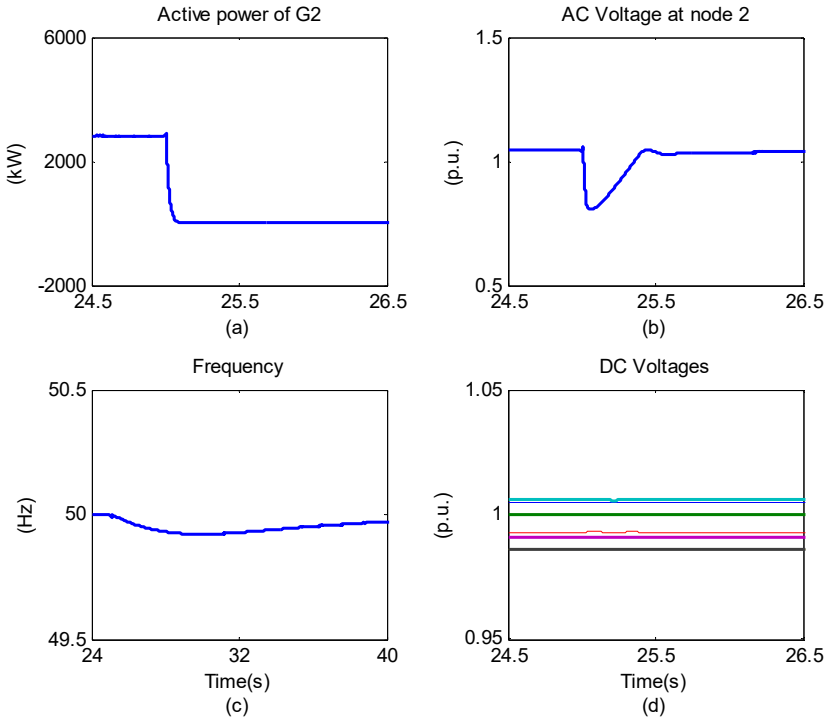

Figure 19. Transients of the system when outage of generator 1 occurs: (**a**) active powers of G2; (**b**) dynamics of the AC voltage at node 2; (**c**) dynamics of the system frequency; (**d**) DC voltage profiles.

B. DC-side faults

Figure 21 shows the transients of the system when a trip of DC line 37 happens at a time of 25 s, while Figure 22 shows the transients when an outage of VSC_1 occurs by opening the AC-side breaker. It is seen that DC voltage first reduces in contrast to AC

voltage at node 1 increasing due to a lack of active power from VSC_1. Then, DC voltages fully recover thanks to the droop control scheme. Oscillations are observed for all DC bus voltages.

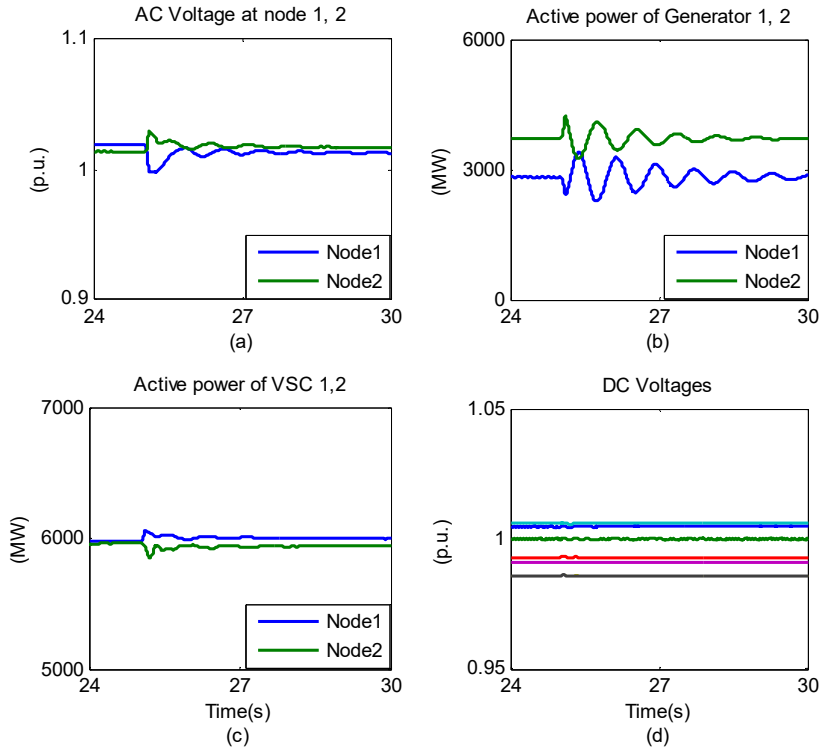

Figure 20. An outage of the AC line 12 in the AC network. (**a**) dynamics of AC voltage at nod 1, 2 (**b**) dynamics of active power of generator 1,2; (**c**) active powers of VSC 1,2;(**d**) DC voltage profiles.

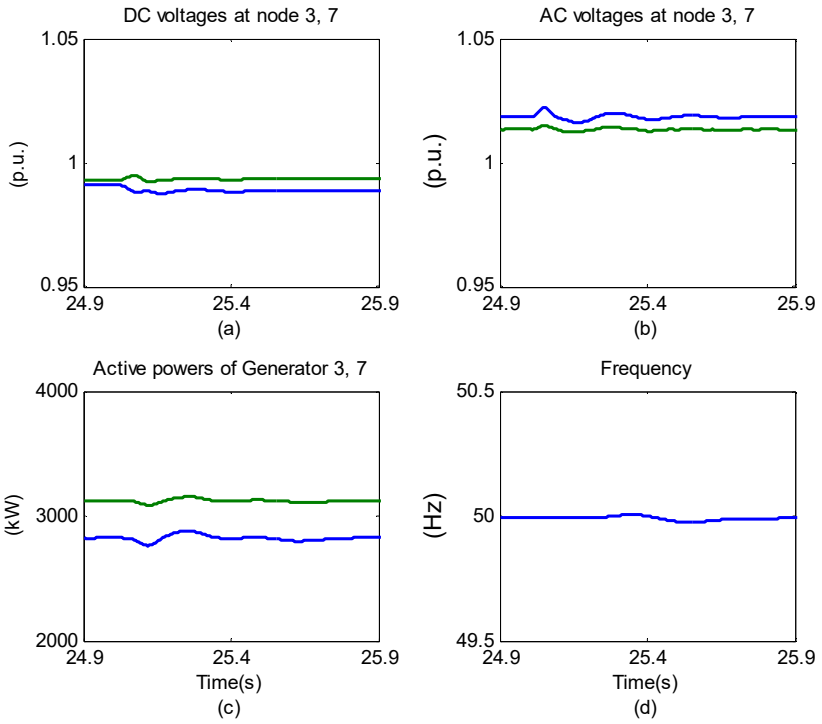

Figure 21. Transients of the system when trip of DC line 37 occurs: (**a**) DC voltages at node 3, 7; (**b**) AC voltages at node 3, 7; (**c**) active powers of generators 3, 7; (**d**) dynamics of the system frequency.

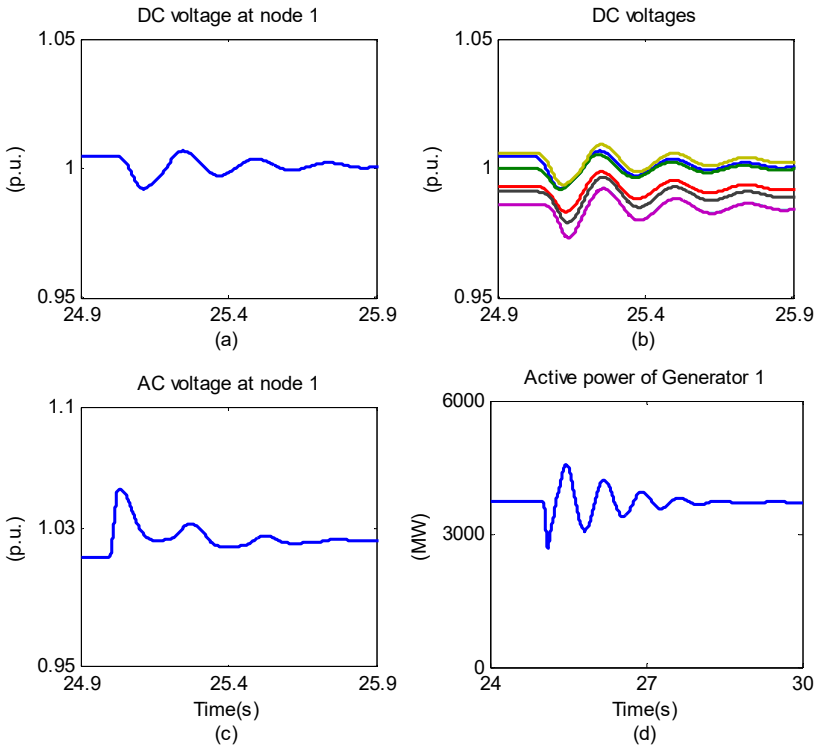

Figure 22. Transients of the system when outage of VSC_1 occurs: (**a**) DC voltage at node 1; (**b**) DC voltages profiles; (**c**) AC voltage at node 1; (**d**) active power of generator 1 [15].

5. Conclusions

In this work, the proposed adaptive control of a multi-VSC-HVDC network to realize maximum voltage support capacity of VSC while ensuring not to make the system frequency worse during severe faults was presented. As a consequence, the enhancement of the voltage stability by the VSC-HVDC network can be obtained. A VSC-HVDC link integrated into the AC system model has been developed based on the electric power transmission grid in south Germany. Several test cases, especially one of the most stressed faults: a three-phase short-circuit in the AC network, were simulated to verify the effective performance of the proposed dynamic reactive power booster scheme. Therefore, the proposed control method makes a contribution to improve the voltage stability of the system in comparison with the traditional control method. It was shown that the automatic utilization of the VSC capacity based on its available headroom for supplying the reactive power is especially essential during serious AC voltage falls to enhance the stability of the system. Furthermore, once the voltage recovery is achieved, the actual reactive current returns to the normal value quickly and the adaptive controller releases the control margin to the active current. After that, the operation of the VSC tracks back to the original operation point, and the output active and reactive power of VSC come back to the planed nominal values, as in the previous schedule. Nevertheless, once the severe fault happens, the output active power of VSC reduces while ensuring this reduction does not make the system frequency lower than the minimum acceptable value. Hence, the output reactive power of VSC increases to support voltage under voltage drops. Therefore, the proposed adaptive control method does not impose further problems involving the frequency stability of the system. Last but not least, the dynamic reactive power booster applied to the multi-VSC-HVDC system can work locally but also support global problems of the AC system integrated to the multi-VSC-HVDC system.

Funding: This research received no external funding.

Acknowledgments: The author further like to acknowledge Kai Strunz for his dedicated supervision and also thanks to Electric Power University for administrative support.

Conflicts of Interest: The authors declare no conflict of interest.

Nomenclature

Acronyms

AC	Alternating Current
BPA	Blade Pitch Angle
CB	Circuit Breaker
CCCS	Current-Controlled Current Source
DC	Direct Current
EMTP	Electromagnetic Transients Program
HVDC	High-Voltage Direct Current
IGBT	Insulated Gate Bipolar Transistor
MPPT	Maximum Power Point Tracking Control
PCC	Point of Common Coupling
PMSG	Permanent Magnet Synchronous Generator
PLL	Phase-Locked Loop
PSCAD	Power System Computer-Aided Design
RES	Renewable Energy Source
TSR	Tip Speed Ratio
UPS	Uninterruptible Power Supply
VCVS	Voltage-Controlled Voltage Source
VCO	Voltage-Controlled Oscillator
VSC	Voltage Source Converter
WECS	Wind Energy Conversion System

Variables

c	Capacitance
C_f	Capacitance in the AC filter
C_p	Performance coefficient
d	Duty ratio
F	Turbulence scale, chosen as 2000
f	Frequency of the system
$f_{\min}$	Permitted minimum frequency of the system
f_{sys}^0	Nominal frequency of the system
f_{sample}	Sample frequency that actual rotor speed is measured
H	Rotational inertia constant of the generator and turbine in WECS
H(p)	Transfer function in the PLL control system
i, j, k, m, n	Counters
i	Instantaneous current
I	Root mean square (RMS) current
i_{dlim}, i_{qlim}	Active and reactive current limit of the current limiter for VSC
i_{dcomp}	A current signal compared with the active current i_{d0}
i_{df}	A current margin that can be reduced depending on frequency
i_{lim}	Maximum current of the VSC
i_{rated}	Rated current of the VSC
K_f	Variable representing the ability of the system to support active power in primary control
$K_{\text{I,dq}}$	Integral components in PI controllers in dq-axis
K_{N}	Surface drag coefficient
K_{lim}	Variable representing the ability of VSC for the overcurrent trip
$K_{\text{P\_opt}}$	Optimum power coefficient constant of PMSG
$K_{\text{P,dq}}$	Proportional components in PI controllers in dq-axis
L	Inductance
L_{md}	Inductance in d-axis
L_{mq}	Inductance in q-axis

L_{ls}	Stator leakage inductance
MAXR	Ramp maximum in m/s
M_d	Control signal in d-axis in a speed controller of PMSG
M_q	Control signal in q-axis in a speed controller of PMSG
P_e	Electric power of PMSG
P_m	Mechanical power of PMSG
P_L	Power of load
P_{sys}^0	Generated active power of the system before disturbance
$P_{sys,max}$	Maximum active power that the system can generate in primary control
Q	Reactive power
$q(t)$	Switching function
R	Resistance
R_L	Resistance of load
R_{tb}	Radius of the wind turbine blades
r_{on}	Switch on-state resistance of VSC
T_m	Mechanical torque of PMSG
T_e	Electromagnetic torque of PMSG
T_{rated}	Rated torque of PMSG
T_G	Gust period
T_{lG}	Gust peak
T_{1R}	Ramp start time
T_{2R}	Ramp max time
v	Instantaneous voltage
V	Root mean square (RMS) voltage
V_{ctrl_d}	A signal control in the current-controlled VSC in d-axis
V_{ctrl_q}	A signal control in the current-controlled VSC in q-axis
$V_{s,abc}$	Three-phase voltage at the PCC
$V_{t,abc}$	Three-phase voltage at the terminal of VSC
V_{tip}	Linear blade tip speed
V_w	Wind speed
V_{WB}	Base wind velocity
V_{WG}	Gust wind component
V_{WR}	Ramp wind component
V_{WN}	Noise wind component
β	Blade pitch angle (BPA) of the turbine blades
ω	Angular frequency
ω_0	The AC system frequency
ω_m	Mechanical rotational speed of the turbine in WECS
ω_r	Rotor rotational speed of PMSG
ω_{r_opt}	Optimum rotor angle speed of PMSG
λ	Tip speed ratio (TSR)
θ	Angular position
θ_0	The initial phase angle
ϕ_1	Angle between currents and voltages
ϕ_i	A random variable with uniform probability density on the interval 0 to 2π
μ	Mean speed of wind at reference height
ρ_a	Air density
ρ	Output of the control block of the PLL
ψ_f	Permanent magnetic flux of PMSG
ζ	Dummy variable of integration

Appendix A. Development of a Representative AC Network Based on the Existing AC System in Germany

In this section, a more detailed representative AC network based on the existing AC system in Germany is developed to provide data of the test case in Figure 1. In order to analyze the interaction between the multi-terminal VSC-HVDC and the AC system, it is

required to develop a more detailed AC system model. However, up to now, there are still some limitations for doing so.

Firstly, it is difficult to have a realistic system as electric power companies are unwilling to provide detailed data of their systems.

Secondly, electromagnetic simulation programs such as PSCAD/EMTDC can accurately simulate dynamic behaviors of a VSC-based HVDC system. However, for large electric power systems, it requires large amounts of calculations, and such large-scale power system simulations are quite slow. In order to solve this problem, there are typically some suggested methods: an electromechanical–electromagnetic hybrid simulation, a FAST method [41], or use the dynamical equivalence of the AC system to reduce the scale for electromagnetic transient simulation.

In the scope of the research, the method to develop a reduced AC network is employed. Namely, in this section, the German AC transmission network will be studied. Finally, the more detailed representative AC system with overlay highway HVDC networks based on multi-terminal VSC is achieved. Since the detailed data are not publicly available, the approximate 220 and 380 kV network is considered. For the creation of the reduced network, determination of main network areas is based on geographical location, population density, vertical load density, wind installed capacity, and thermal plant installed capacity. Local nodes are merged, and the resulting nodes should represent the original nodes, while key nodes should be recognizable among the resulting nodes. Some groups of closely connected buses are merged into one equivalent bus to ensure that bus represents the main node of the selected area. Each area is represented by one main node and main bus. Resulting transmission lines should reflect transmission capacities and their limitations. The new line lengths are calculated on the basic data of the network. It is approximated that for a single circuit 380 and 220 kV system, the impedance values are 0.028 + j0.25 and 0.109 + j0.31 ohm/km at a frequency of 50 Hz [42]. The data of loads are gathered according to data of the UCTE area in [43]. The data of power plants as well as wind energy sources are collected according to global data [44]. The exchange powers to other countries are regarded as positive or negative supplies. As a result, the more detailed representative AC system based on Germany is shown in Figure A1. A summary of the basic data of the regional sub-areas is described in Table A1. Other parameters of the more realistic AC are provided in Tables A3 and A4.

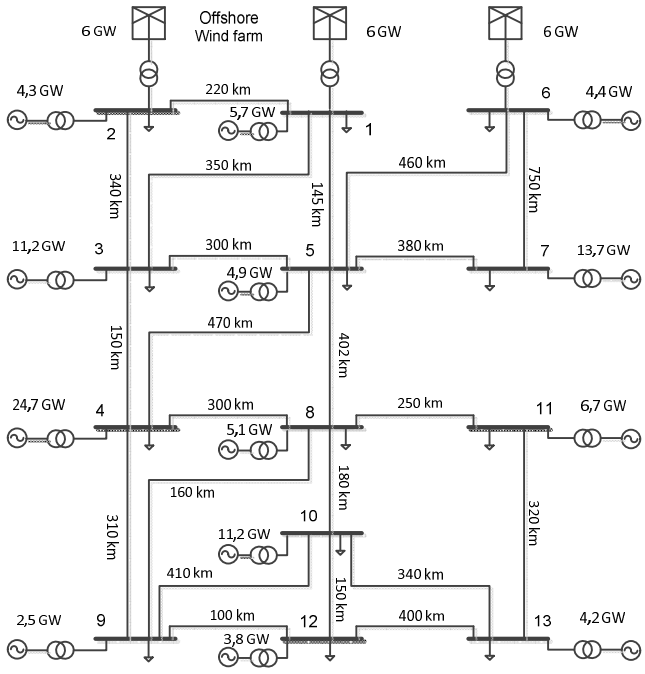

Figure A1. The more detailed representative AC system.

Table A1. Summary of the basic data of the represented areas.

Areas	Installed Capacity (MW)	Vertical Network Load (%)	Wind Installed Capacity (%)
Area 1	5701	7.27	11.61
Area 2	4339	4.02	24.21
Area 3	11,196	6.71	5.59
Area 4	24,749	22.87	7.12
Area 5	4883	5.32	3.35
Area 6	4426	8.25	23.14
Area 7	13,731	6.98	10.46
Area 8	5064	8.16	5.12
Area 9	2470	4.21	5.72
Area 10	11,182	5.97	0.66
Area 11	6699	5.66	1.19
Area 12	3839	5.83	0.84
Area 13	4236	8.75	0.99
Total	**102,515**	**100**	**100**

Appendix B. Modeling of Wind Farm

In this section, the mathematical model of a wind farm used in the study is briefly presented. The generator used in WECS for this research is a permanent magnet synchronous generator (PMSG). With the maximum power point tracking (MPPT) control, the generator enables operation of the wind turbine at its maximum power coefficient over a wide range of wind speeds, thereby capturing optimal energy from the wind [45]. The PMSG is connected to a DC bus through an AC/DC converter. The state space model of the WECS is derived from [45–47]. Details of the modeling of a wind farm is presented in [22]. Only derived equations are presented here to help readers.

Appendix B.1. Wind Speed Model

In order to provide wind speed for the study, the wind speed model chosen for this study is a four-component model and is defined by the following equations [48]:

$$V_{\mathrm{W}} = V_{\mathrm{WB}} + V_{\mathrm{WG}} + V_{\mathrm{WR}} + V_{\mathrm{WN}} \tag{A1}$$

$V_{\mathrm{WG}} = V_{\cos}$ when $T_{1\mathrm{G}} < t < T_{1\mathrm{G}} + T_{\mathrm{G}}$ otherwise $V_{\mathrm{WG}} = 0$.

$$V_{\cos} = (MAXG/2)\{1 - \cos(2\pi(t/T_{\mathrm{G}}) - (T_{1\mathrm{G}}/T_{\mathrm{G}}))\} \tag{A2}$$

$V_{\mathrm{WR}} = V_{\mathrm{ramp}}$ when T1R < t <T2R otherwise $V_{\mathrm{WR}} = 0$. where:

$$V_{\mathrm{ramp}} = MAXR[1 - (t - T_{2\mathrm{R}})/(T_{1\mathrm{R}} - T_{2\mathrm{R}})] \tag{A3}$$

$$V_{\mathrm{WN}} = 2\sum_{i=1}^{N}[S_{\mathrm{V}}(\omega_i)\Delta\omega]^{1/2}\cos(\omega_i t + \phi_i), t < 0$$

$$S_V(\omega_i) = \frac{2K_{\mathrm{N}}F^2|\omega_i|}{\pi^2[1 + (F\omega_i/\mu\pi)^2]^{4/3}}$$

Appendix B.2. Model of Wind Turbine

$$P_{\mathrm{m}} = \frac{1}{2}\rho_{\mathrm{a}} A_{\mathrm{st}} V_{\mathrm{w}}^3 C_{\mathrm{p}}(\beta, \lambda) \tag{A4}$$

$$\lambda = \frac{V_{\mathrm{tip}}}{V_{\mathrm{m}}} = \frac{R_{\mathrm{tb}}\omega_{\mathrm{m}}}{V_{\mathrm{m}}} \tag{A5}$$

$$T_{\mathrm{m}} = \frac{1}{2\lambda}\rho_{\mathrm{a}} \pi R_{\mathrm{tb}}^3 V_{\mathrm{w}}^2 C_{\mathrm{p}} \tag{A6}$$

$$C_{\mathrm{p}}(\beta, \lambda) = 0.73\left(\frac{151}{\lambda_{\mathrm{t}}} - 0.58\beta - 0.002\beta^{2.14} - 13.2\right)e^{-\frac{18.4}{\lambda_{\mathrm{t}}}} \tag{A7}$$

$$\lambda_{\mathrm{t}} = \frac{1}{\frac{1}{\lambda - 0.02\beta} - \frac{0.003}{\beta^3 + 1}} \tag{A8}$$

$$\dot{\omega}_{\mathrm{r}} = \frac{1}{2HT_{\mathrm{rated}}}(T_{\mathrm{m}} - T_{\mathrm{e}}) \tag{A9}$$

$$T_{\mathrm{rated}} = \frac{P_{\mathrm{gen\_rated}}}{\omega_{\mathrm{r\_rated}}} \tag{A10}$$

Appendix B.3. Model of Wind Generator and Its Control System

The model of the PMSG generator is established in a *dq0* reference frame synchronously rotating and aligned with the rotor. The q-axis is 90° ahead of the d-axis with respect to the direction. The state space model of the PMSG can be written as:

$$\dot{i}_{\mathrm{d}} = \frac{1}{L_{\mathrm{md}} + L_{\mathrm{ls}}}(-R_{\mathrm{s}} i_{\mathrm{d}} + \omega_{\mathrm{e}}(L_{\mathrm{mq}} + L_{\mathrm{ls}}) i_{\mathrm{q}} + u_{\mathrm{d}}) \tag{A11}$$

$$\dot{i}_{\mathrm{q}} = \frac{1}{L_{\mathrm{mq}} + L_{\mathrm{ls}}}(-R_{\mathrm{s}} i_{\mathrm{q}} - \omega_{\mathrm{e}}(L_{\mathrm{md}} + L_{\mathrm{ls}}) i_{\mathrm{d}} - \omega_{\mathrm{e}}\psi_{\mathrm{f}} + u_{\mathrm{q}}) \tag{A12}$$

$$T_{\mathrm{e}} = 1.5p((L_{\mathrm{md}} - L_{\mathrm{mq}}) i_{\mathrm{d}} i_{\mathrm{q}} + \psi_{\mathrm{f}} i_{\mathrm{q}}) \tag{A13}$$

$$u_{\mathrm{d}} = d_{\mathrm{d}} V_{\mathrm{dc}} \tag{A14}$$

$$u_{\mathrm{q}} = d_{\mathrm{q}} V_{\mathrm{dc}} \tag{A15}$$

$$\dot{i}_{\mathrm{d}} = \frac{1}{L_{\mathrm{md}} + L_{\mathrm{ls}}}(-R_{\mathrm{s}} i_{\mathrm{d}} + \omega_{\mathrm{e}}(L_{\mathrm{mq}} + L_{\mathrm{ls}}) i_{\mathrm{q}} + d_{\mathrm{d}} V_{\mathrm{dc}}) \tag{A16}$$

$$\dot{i}_{\mathrm{q}} = \frac{1}{L_{\mathrm{mq}} + L_{\mathrm{ls}}}(-R_{\mathrm{s}} i_{\mathrm{q}} - \omega_{\mathrm{e}}(L_{\mathrm{md}} + L_{\mathrm{ls}}) i_{\mathrm{d}} - \omega_{\mathrm{e}}\psi_{\mathrm{f}} + d_{\mathrm{q}} V_{\mathrm{dc}}) \tag{A17}$$

$$\omega_{\mathrm{r\_opt}} = \sqrt[3]{\frac{P_{\mathrm{gen}}}{K_{\mathrm{P\_opt}}}} \tag{A18}$$

$$M_{\mathrm{dP}} = K_{\mathrm{P1}}(i_{\mathrm{dref}} - i_{\mathrm{d}}) \tag{A19}$$

$$\dot{M}_{\mathrm{dI}} = K_{\mathrm{I1}}(i_{\mathrm{dref}} - i_{\mathrm{d}}) \tag{A20}$$

$$M_{\mathrm{d}} = M_{\mathrm{dP}} + M_{\mathrm{dI}} \tag{A21}$$

$$V_{\mathrm{ctr,d}} = 2(\omega_{\mathrm{e}}(L_{\mathrm{mq}} + L_{\mathrm{ls}}) i_{\mathrm{q}})/V_{\mathrm{dc}} \tag{A22}$$

$$V_{\mathrm{ctr,q}} = 2(\omega_{\mathrm{e}}(L_{\mathrm{mq}} + L_{\mathrm{ls}}) i_{\mathrm{d}} + \omega_{\mathrm{e}}\psi_{\mathrm{f}})/V_{\mathrm{dc}} \tag{A23}$$

$$d_{\mathrm{d}} = M_{\mathrm{d}} - \frac{2(\omega_{\mathrm{e}}(L_{\mathrm{mq}} + L_{\mathrm{ls}}) i_{\mathrm{q}})}{V_{\mathrm{dc}}} \tag{A24}$$

$$i_{\mathrm{qrefP}} = K_{\mathrm{P2a}}(\omega_{\mathrm{r\_opt}} - \omega_{\mathrm{r}}) \tag{A25}$$

$$\dot{i}_{\mathrm{qrefI}} = K_{\mathrm{I2a}}(\omega_{\mathrm{r\_opt}} - \omega_{\mathrm{r}}) \tag{A26}$$

$$i_{\mathrm{qref}} = i_{\mathrm{qrefP}} + i_{\mathrm{qrefI}} \tag{A27}$$

$$M_{\mathrm{qP}} = K_{\mathrm{P2b}}(i_{\mathrm{qref}} - i_{\mathrm{q}}) \tag{A28}$$

$$\dot{M}_{\mathrm{qI}} = K_{\mathrm{I2b}}(i_{\mathrm{qref}} - i_{\mathrm{q}}) \tag{A29}$$

$$M_{\mathrm{q}} = M_{\mathrm{qP}} + M_{\mathrm{qI}} \tag{A30}$$

$$d_{\mathrm{q}} = M_{\mathrm{q}} + \frac{2(\omega_{\mathrm{e}}(L_{\mathrm{mq}} + L_{\mathrm{ls}})i_{\mathrm{d}} + \omega_{\mathrm{e}}\psi_{\mathrm{f}})}{V_{\mathrm{dc}}} \tag{A31}$$

$$\beta_1 = K_{\mathrm{P}}(\max(P_{\mathrm{gen}}, P_{\mathrm{gen\_rated}}) - P_{\mathrm{gen\_rated}}) \tag{A32}$$

$$\beta_{2\mathrm{P}} = K_{\mathrm{P3}}(\omega_{\mathrm{r}} - \omega_{\mathrm{r\_rated}}) \tag{A33}$$

$$\dot{\beta}_{2\mathrm{I}} = K_{\mathrm{I3}}(\omega_{\mathrm{r}} - \omega_{\mathrm{r\_rated}}) \tag{A34}$$

$$\beta_2 = \beta_{2\mathrm{P}} + \beta_{2\mathrm{I}} \tag{A35}$$

$$\beta = \beta_1 + \beta_2 \tag{A36}$$

Appendix C. Simulation Parameters of the Case Studies

Table A2. Parameters of HVDC cables.

"From" Node	"To" Node	Voltage (kV)	Distance (km)	System
1	2	800	197	4
2	3	800	136	4
3	4	800	259	4
4	5	800	574	4
5	6	800	336	4
5	1	800	384	4
6	7	800	217	4
7	1	800	460	2

Table A3. Data of the reduced AC network.

Representing Bus	Real Bus	Name
1	132	Hamburg Ost
2	145	Conneforde
3	218	Unna
4	249	Dortmund
5	305	Wahle
6	52	Lubmin
7	106	Vieselbach
8	335	Grafenrhein feld
9	379	Abzweig Koblenz
10	429	Heilbronn
11	443	Reitersaich
12	467	Hoheneck
13	548	Ottenhofen

Table A4. Parameters of the AC lines in the reduced network.

Lines	**1–2**	**1–3**	**1–5**	**2–3**	**3–4**	**3–5**
Length (km)	220	347.5	145	340	150	300
Lines	4–8	4–9	4–5	5–7	5–8	6–7
Length (km)	302	310	470	380	402	750
Lines	6–5	8–10	8–11	8–9	9–10	9–12
Length (km)	460	180	250	160	410	100
Lines	10–12	10–13	11–13	12–13		
Length (km)	150	340	320	400		

Table A5. Parameters of VSC-HVDC networks.

Rated capacity	6000 MVA
Active power delivered	4800 MW
DC voltage	800 kV
Base capacity	6000 MVA
Base DC voltage	800 kV

Table A6. Parameters of the induction motor.

Location	Bus 13
Capacity	4000 MVA
Power factor	0.75
Inertia	3.412 s

Table A7. Parameters of PMSG.

Description	**Nominal Power**	**Nominal Mechanical Speed**	**Pole Pairs**
Notation	$P_{\text{gen\_rated}}$	$\omega_{\text{r\_rated}}$	p
Value (unit)	2 MW	2.18 rad/s	11
Description	Generator, Turbine inertia constant	Permanent magnet flux	Stator q-axis inductance
Notation	H	ψ_{f}	L_{md}
Value (unit)	3 sec	136 Wb	0.334 H
Description	Stator d-axis inductance	Stator leakage inductance	Stator resistance
Notation	L_{mq}	L_{ls}	R_{s}
Value (unit)	0.217 H	0.0334 H	0.08 Ω

Table A8. Parameters of controllers of PMSG.

Gain	K_{p1}	K_{I1}	K_{p2a}	K_{I2a}	K_{P2b}	K_{I2b}	K_{P3}	K_{I3}	K_{P}
Value	101	221	0.05	1.5	101	221	2	4	2

References

1. Alassi, A.; Banales, S.; Ellabban, O.; Adam, G.; MacIver, C. HVDC Transmission: Technology Review, Market Trends and Future Outlook. *Renew. Sustain. Energy Rev.* **2019**, *112*, 530–554. [CrossRef]

2. Bernat, O.; Preece, R. Impact of VSC-HVDC Reactive Power Control Schemes on Voltage Stability. In Proceedings of the 2019 IEEE Milan PowerTech, Milan, Italy, 23–27 June 2019.
3. Ishfaq, M.; Uddin, W.; Zeb, K.; Islam, S.U.; Hussain, S.; Khan, I.; Kim, H.J. Active and Reactive Power Control of Modular Multilevel Converter Using Sliding Mode Controller. In Proceedings of the Conference on Computing, Mathematics and Engineering Technologies (iCoMET), ISukkur, Pakistan, 30–31 January 2019.
4. Renedo, J.; Garcia-Cerrada, A.; Rouco, L. Reactive-Power Coordination in VSC-HVDC Multi-Terminal Systems for Transient Stablity Improvement. *IEEE Trans. Power Syst.* **2017**, *32*, 3758–3767. [CrossRef]
5. Shen, Y.; Yao, W.; Wen, J.Y.; He, H.; Chen, W. Adaptive Supplementary Damping Control of VSC-HVDC for Interarea Oscillation Using GrHDP. *IEEE Trans. Power Syst.* **2018**, *33*, 1777–1789. [CrossRef]
6. Guo, C.; Zhao, C. Supply of an entirely passive AC network through a double-infeed HVDC system. *IEEE Trans. Power Electron.* **2010**, *25*, 2835–2841.
7. Du, C.; Agneholm, E.; Olsson, G. VSC-HVDC system for industrial plants with onsite generators. *IEEE Trans. Power Deliv.* **2009**, *24*, 1359–1366. [CrossRef]
8. Nikkhajoei, K.H.; Iravani, R. Control of an Electronically-Coupled Distributed Resource Unit Subsequent to an Islanding Event. *IEEE Trans. Power Deliv.* **2008**, *23*, 493–501. [CrossRef]
9. Kotb, O.; Ghandhari, M.; Eriksson, R.; Leelaruji, R.; Sood, V.K. Stability enhancement of an interconnected AC/DC power system through VSC-MTDC operating point. *J. Electr. Power Syst. Res.* **2017**, *151*, 308–318. [CrossRef]
10. Wang, T.; Zhou, Y.; Li, D.; Shao, D.; Cao, K.; Zhou, K.; Cai, D. The Influence of VSC-HVDC Reactive Power Control Mode on AC Power System Stability. *Energies* **2020**, *13*, 1677. [CrossRef]
11. Shah, R.; Preece, R.; Barnes, M. The Impact of Voltage Regulation of Multi-infeed VSC-HVDC on Power System Stability. *IEEE Trans. Energy Convers.* **2018**, *33*, 1614–1627. [CrossRef]
12. Liu, Y.; Chen, Z. A Flexible Power Control Method of VSC-HVDC Link for the Enhancement of Effective Short-Circuit Ratio in a Hybrid Multi-Infeed HVDC System. *IEEE Trans. Power Syst.* **2013**, *28*, 1568–1581. [CrossRef]
13. Ajaei, F.B.; Iravani, R. Dynamic interactions of the MMC-HVDC grid and its host AC system due to AC-side disturbances. *IEEE Trans. Power Deliv.* **2016**, *31*, 1289–1298. [CrossRef]
14. Huu, D.N. A Coordinated Protection Scheme of multi-terminal VSC-HVDC links under DC faults. In Proceedings of the 2016 IEEE Innovative Smart Grid Technologies—Asia (ISGT-Asia), Melbourne, VIC, Australia, 28 November–1 December 2016.
15. Huu, D.N. Modeling and Analysis of an integrated AC-DC network under AC and DC faults. In Proceedings of the 2016 IEEE International Conference on Sustainable Energy Technologies (ICSET), Hanoi, Vietnam, 14–16 November 2016.
16. Huu, D.N. Small signal assessment of an AC system integrated with a VSC-HVDC network. In Proceedings of the IEEE EUROCON, Salamanca, Spain, 8–11 September 2015.
17. Laures, W. Untersuchungen zum Einsatz von Höchstspannungskabeln großer Längen in der 400-kV-Ebene. Ph.D. Thesis, Universität Duisburg-Essen, Duisburg, Germany, 2003.
18. Wu, T.F.; Chang, C.H.; Lin, L.C.; Yu, G.; Chang, Y.R. DC-Bus Voltage Control With a Three-Phase Bidirectional Inverter for DC Distribution Systems. *IEEE Trans. Power Electron.* **2013**, *28*, 1890–1899. [CrossRef]
19. Mishra, M.K.; Karthikeyan, K. A Fast-Acting DC-Link Voltage Controller for Three-Phase DSTATCOM to Compensate AC and DC Loads. *IEEE Trans. Power Deliv.* **2009**, *24*, 2291–2299. [CrossRef]
20. Delghavi, M.B.; Yazdani, A. Islande-Mode Control of Electronically Coupled Distributed-Resource Units under Unbalanced and Nonlinear Load Conditions. *IEEE Trans. Power Deliv.* **2011**, *26*, 661–673. [CrossRef]
21. Yazdni, A.; Iravani, R. *Voltage-Sourced Converters in Power Systems*; IEEE Press: Piscataway, NJ, USA; John Wiley & Sons, Inc.: Hoboken, NJ, USA, 2010.
22. Huu, D.N. State-Space Modelling and Voltage Control of AC-DC Networks. Ph.D. Thesis, Technical University of Berlin, Berlin, Germany, 2014.
23. IEEE. *IEEE Recommended Practice for Excitation System Models for Power System Stability Studies*; IEEE Std. 421.5-1992; IEEE: Piscataway, NJ, USA, 1992.
24. Trebincevic, I.; Malik, O.P. Computer Models for Representation of Digital-Based Excitation Systems. *IEEE Trans. Energy Convers.* **1996**, *11*, 607–615.
25. Mover WG, P.; Supply, E. Hydraulic Turbine and Turbine Control Models for System Dynamic Studies, Working Group on Prime Mover and Energy Supply Models for System Dynamic Performance Studies. *Trans. Power Syst.* **1992**, *7*, 167–179.
26. Kundur, P. *Power System Stability and Control*; McGraw Hill Inc.: New York, NY, USA, 1994.
27. Manitoba HVDC Research Centre, Tech. Rep. EMTDC Transient Analysis for PSCAD Power System Simulation Version 4.2.0. Available online: https://hvdc.ca/ (accessed on 31 May 2021).
28. Prysmian Cables and Systems B.V. High Voltage Cables. Available online: www.prysmian.com (accessed on 3 September 2013).
29. Angquist, L.; Lindberg, L. Inner Phase Angle Control of Voltage Source Converter in High Power Applications. In Proceedings of the IEEE Power Electronics Specialists Conference PESC 91, Cambridge, MA, USA, 24–27 June 1991; pp. 293–298.
30. Xu, L.; Agelidis, V.G.; Acha, E. Development Considerations of DSP Controlled PWM VSC-Based STATCOM. *IEEE Proc. Electr. Power Appl.* **2001**, *148*, 449–455. [CrossRef]
31. Bergen, A.R. *Power System Analysis*; Prentice-Hall: Hoboken, NJ, USA, 1986.

32. Kazmierkowski, M.; Malesani, L. Current-Control Techniques for Three Phase Voltage-Source PWM Converters: A survey. *IEEE Trans. Ind. Electron.* **1998**, *45*, 691–703. [CrossRef]
33. Temesgen, M.H.; Uhlen, K. Impact of DC line Voltage Drops on Power Flow of MTDC Using Droop Control. *IEEE Trans. Power Syst.* **2012**, *27*, 1441–1449.
34. Hendriks, R.L.; Paap, G.C.; Kling, W.L. Control of a multi-terminal VSC Transmission scheme for interconnecting offshore wind farms. In Proceedings of the Europe Wind Energy Conference Exhibition, Milan, Italy, 7–10 May 2007; pp. 1–8.
35. Xu, L.; Williams, B.W.; Yao, L. Multi-terminal DC transmission systems for connecting large offshore wind farms. In Proceedings of the IEEE PES General Meeting—Conversion and Delivery of Electrical Energy in the 21st Century, Pittsburgh, PA, USA, 20–24 July 2008; pp. 1–7.
36. Autobahnen 1-999. 2005. Available online: http://www.autobahnatlas-online.de (accessed on 2 October 2012).
37. da Silva, R.; Teodorescu, R.; Rodriguez, P. Power delivery in MTDC transmission system for offshore wind power applications. In Proceedings of the IEEE PES ISGT Europe, Gothenburg, Sweden, 11–13 October 2010; pp. 1–8.
38. Lu, W.; Ooi, B.-T. Multi-terminal HVDC as enabling technology of premium quality power park. *IEEE PES Winter Meet.* **2002**, *2*, 719–724.
39. Delghavi, M.B.; Yazdani, A. A Control Strategy for Islanded Operation of a Distributed Resource (DR) Unit. *IEEE Power Energy Soc. Gen. Meet.* **2008**, *7*, 20–24.
40. Du, C. The Control of VSC-HVDC and Its Use for Large Industrial Power Systems. Thesis for the Degree of Licentiate of Engineering, Göteborg, Sweden, 2003.
41. Strunz, K.; Shintaku, R.; Gao, F. Frequency-Adaptive Network Modeling for Integrative Simulation of Natural and Envelope Waveforms in Power Systems and Circuits. *IEEE Trans. Circuits Syst.* **2006**, *53*, 2788–2803. [CrossRef]
42. Say, M.G. *Electrical Engineer's Reference Book*, 13th ed.; Butterworth: London, UK, 1973.
43. Zhou, Q.; Bialek, J.W. Approximate model of European interconnected system as a benchmark system to study effects of cross-border trades. *IEEE Trans. Power Syst.* **2005**, *20*, 782–788. [CrossRef]
44. UCTE. *UCTE Interconnected Network*; UCTE: Brussels, Belgium, 2008.
45. Strachan, N.P.W.; Jovcic, D. Dynamic modeling, simulation and analysis of an offshore variable-speed directly-driven permanent-magnet wind energy conversion and storage system (WECSS). In Proceedings of the OCEANS 2007-Europe, Aberdeen, Scotland, 18–21 June 2007.
46. Slootweg, J.G.; De Haan, S.W.H.; Polinder, H.; Kling, W.L. General Model for Representing Variable Speed Wind Turbines in Power System Dynamics Simulations. *IEEE Trans. Power Systems* **2003**, *8*, 144–151. [CrossRef]
47. Chinchilla, M.; Arnaltes, S.; Burgos, J.C. Control of Permanent Magnet Generators Applied to Variable-Speed Wind-Energy Systems Connected to the grid. *IEEE Trans. Energy Convers.* **2006**, *21*, 130–135. [CrossRef]
48. Anderson, P.M.; Bose, A. Stability Simulation of Wind Turbine Systems. *IEEE Trans. Power Appar. Syst.* **1983**, *12*, 3791–3795. [CrossRef]